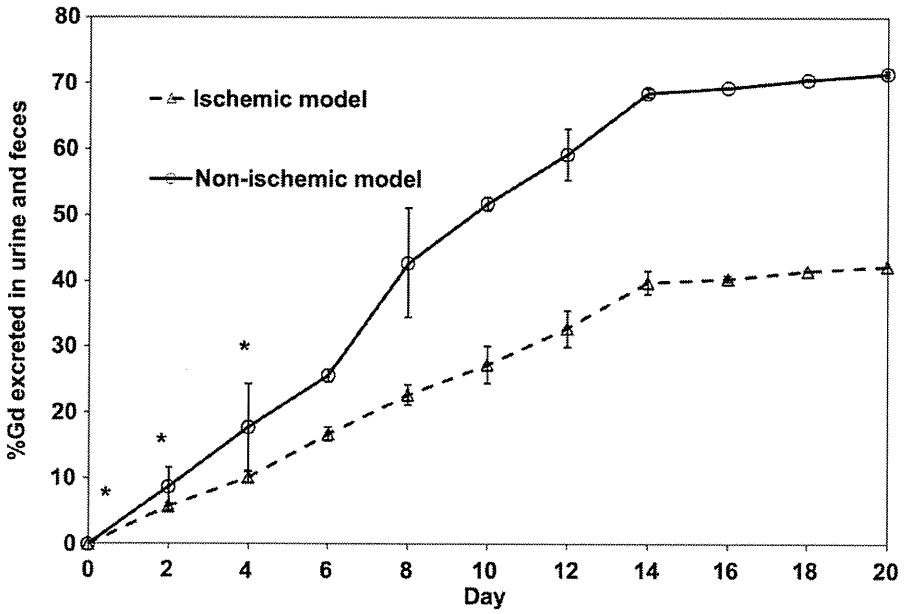

Fig. 5. Clearance of gadolinium (Gd) from the ischemic and non-ischemic models. Total percentage of Gd cleared from urine and feces. EPCs contained 0.83 pg of Gd of a total of 7.8 ± 0.73 μg Gd/rat transplanted in the limb (1.65×10^{-4} mmol/kg body weight). Urine and feces samples were treated with nitric acid before measurement by inductively coupled plasma atomic emission spectroscopy (ICP-AES). Samples were measured in duplicate. Values are mean (±SD) at each time point ($n = 3$). Note: error bars may be smaller than the symbols. No statistically significant differences were detected between day 0 and day 4 after labeled cell implantation; $^*P > 0.05$. The difference was statistically significant from day 6 to day 20, $P < 0.01$.

that are involved in vascular integrity. The VE-cadherin is fundamental for vascular tube formation and participates in cell survival signaling by interaction with beta catenin, VEGF-R2, and PI3 kinase complexes [23]. Flow cytometry showed that the EPC phenotype remained stable after Dex-DOTA-Gd^{3+} labeling by electroporation.

Consistent with our previous study, the results presented herein demonstrated that Dex-DOTA-Gd^{3+} as an MRI contrast agent did not influence the capacity of blood perfusion restoration (Fig. 2A and B), collateral vessel formation (Fig. 2D), and expression of growth factors, which in turn support the survival and function of

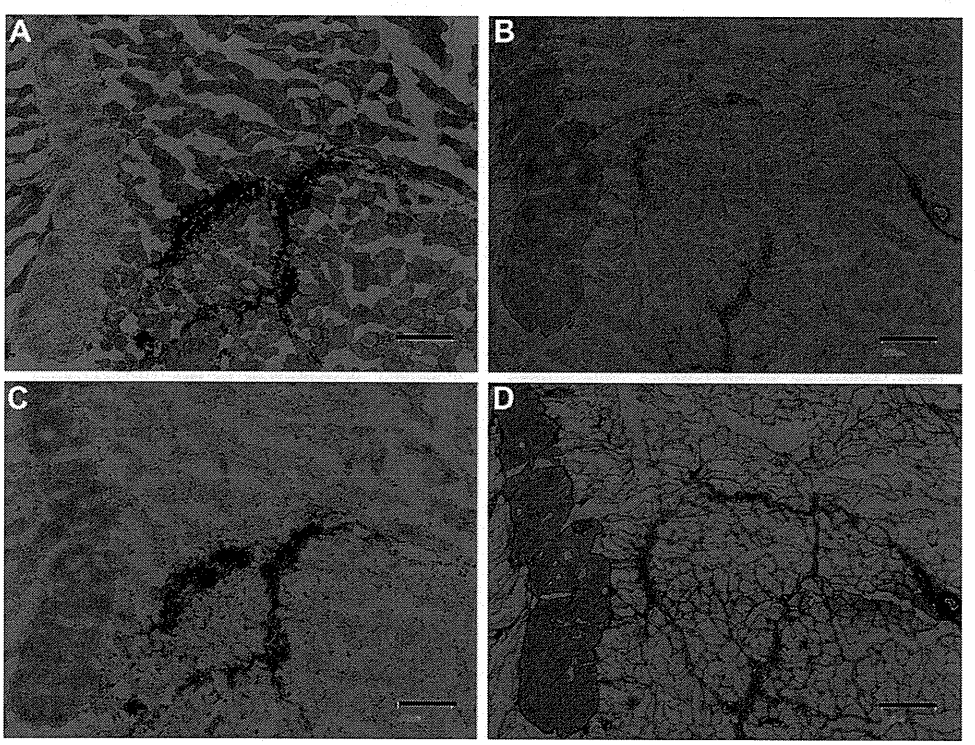

Fig. 6. Representative histology of rat ischemic tissue harvested 21 days after transplantation of SPIO-labeled EPCs. (A) Berlin blue staining shows the presence of large groups of iron-containing cells in an animal implanted with EPCs. (B) CD68 immunostaining showing a large number of positive cells (macrophages) with a pattern similar to that of Berlin blue-positive cells. (C) von Willebrand factor (vWF) and (D) alpha smooth muscle actin (α-SMA)-positive cells in a rat implanted with SPIO-labeled EPCs.

tissue resident cells, and consequently, enhance the vasculogenesis process and regeneration of ischemic limbs [19].

MRI as a high-resolution technique for tracking EPCs in vivo can provide important insights on the different phenomena associated with angiogenesis of ischemic limb models [15–17,22]. In vivo MRIs (Fig. 3B and Supplementary Fig. 2) indicated that Dex-DOTA-Gd^{3+}-labeled EPCs are perfectly detectable and the fate of the cells can be followed within 14 days after transplantation. When acquiring T1-weighted MRIs, Dex-DOTA-Gd^{3+}-labeled EPCs transplanted into an ischemic limb model exhibited a pattern of migration in which cells moved along the adductor in the direction of the knee mobilized by chemoattraction to the foci of vasculogenesis, thus restoring blood perfusion. This particular migration pattern was observed in all of the studied animal models. In contrast, MRIs of Dex-DOTA-Gd^{3+}-labeled EPCs transplanted into a non-ischemic limb model showed a different pattern. Cells were not mobilized from the injection point and remained in that location until they disappeared within 8 days post-transplantation. This is probably due to the absence of chemokines in the non-ischemic model. Dex-DOTA-Gd^{3+}-labeled EPCs could no longer remain alive in the limb, and the contrast agent in the cells was cleared from the body.

In ischemic models implanted with SPIO-labeled EPCs, the anatomic location of labeled cells at the injection point can be efficiently tracked. Despite the fact that EPCs transplanted into ischemic tissues are expected to migrate and be incorporated into vessel structures [21], SPIO-labeled cells did not show migration, and the fate of EPCs could not be monitored in the long term. Remarkably, no differences in the MRI scans could be observed from day 1 to day 21. Further immunohistological analysis at day 21 after cell transplantation identified the SPIO-containing cells as tissue macrophages. The uptake of SPIO by these infiltrated cells led to the persistence of iron at the injection site, which generated the signal on the MRIs. Previous studies demonstrated that transplantation of iron-labeled cells enabled tracking of the cells over time [23,24,41]. However, several studies have found that iron nanoparticles are not consistent markers to track the fate and survival of transplanted labeled stem cells.

Clearance of Gd from the rat models via urine and feces demonstrated that the living Dex-DOTA-Gd^{3+}-labeled EPCs can be tracked over long periods of time, while the contrast agent contained in dead cells is released and cleared from the body. In the ischemic models, 43% of the total Gd incorporated in the labeled cells was gradually cleared via urine and feces within 14 days post-transplantation (Fig. 5), ensuring that the living Dex-DOTA-Gd^{3+}-labeled cells were the only cells tracked by MRI. In non-ischemic models, 74% of the total Gd was progressively excreted, indicating that labeled cells slowly died, thereby releasing the excess label. However, living labeled cells where tracked for about 8 days, were completely banished within 14 days (Fig. 3C, only in model 2), and did not migrate in the ischemic limb. The amount of Gd excreted in the non-ischemic models was higher (31%) than in the ischemic models, suggesting that the Gd clearance profiles are different in the 2 models. These results confirm the reliability of Dex-DOTA-Gd^{3+} as MRI contrast agent for tracking living cells.

The amounts of Gd cleared via urine and feces were separately measured by ICP mass. However, we combined the amounts of Gd from urine and feces (Fig. 5) because despite the use of metabolic cages to separately collect feces and urine, absorption of urine by feces could not be avoided in some cases. Moreover, a significant quantity of urine was attached to and dried in the cage walls and supporting rat meshes. Because we expected all of the Gd incorporated in labeled cells to be released in the non-ischemic models, and because the amount of Gd from kidneys and livers was extremely low in comparison with the total dosage, we assumed that the loss of Gd in the cages amounted to approximately 26.5% of the total (2.1 μg). However, we believe that the loss of Gd in the ischemic models was lower. Despite the limitations in collecting the excrements in animal models, we believe that this method can be applied to clinical trials due to the better control of collecting the excrements, which would allow a more accurate estimation of the total Gd cleared from the body.

Gd ions released from contrast agents have been suspected to play a role in nephrogenic systemic fibrosis (NSF) in patients with primary renal disease [39]. Although Gd ions strongly bind DOTA and form stable chelates [42], the possible presence of free Gd ions cannot be ruled out. To avoid this situation, we used a Gd/DOTA ratio in Dex-DOTA-Gd^{3+} of 0.78; the remaining empty DOTA in the polymer was 0.22 (polymer unit). Consequently, Gd released from the chelates can be captured by the Dex-DOTA-Gd^{3+} complex because of the available DOTA groups near the free Gd ions.

The common clinical dosage of MRI contrast agents is 1800 times higher than the dosage used for Dex-DOTA-Gd^{3+}-labeled stem cells. In addition, the incorporation of DOTA-Gd^{3+} into dextran probably increased the relaxation time due to a steric limitation on the rotational movement of the polymer, which increased the rotational correlation coefficient [42]. Therefore, the quantity of contrast agent necessary to enhance the imaging results is considerably lower than that used in Gd complex contrast agents such as DOTA-Gd^{3+} and Magnevist® which exhibit a relatively slow relaxation time in comparison with Dex-DOTA-Gd.$^{3+}$ [35].

BM-derived Dex-DOTA-Gd^{3+}-labeled EPCs that survived in the ischemic limbs were incorporated into the sites of neovascularization and promoted the collateral vessels formation. Dex-DOTA-Gd^{3+} did not probably affect the mobilization, chemoattraction, or adhesion of EPCs with regard to the regeneration of ischemic tissue.

5. Conclusion

Our results demonstrated the reliability of Dex-DOTA-Gd^{3+} as MRI contrast agent for labeling of BM-derived EPCs by electroporation and tracking of labeled stem cells in ischemic limbs over time. MRI was capable of distinguishing living cells from dead cells because the Dex-DOTA-Gd^{3+} freed from dead cells was rapidly cleared from the body. In contrast, although SPIO was useful for monitoring the anatomic location of labeled cells, it did not provide consistent information on long-term cell viability. The present analysis of MRIs provides evidence of how cell migration occurs along the muscle to the ischemic site, showing a different pattern of migration than that observed in non-ischemic limbs. These achievements in the in vivo assessment of cell migration are a crucial contribution to the advancement of human stem cell-based therapies.

Author contributions

C.A.A., T.Y., and Y.T conceived and designed all studies. A.F.H. and C.A.A. edited the MRI scans. H.I. and T.O. contributed with the implementation of the rat ischemic limb model and MRI studies along with C.A.A. Paper was wrote by C.A.A. All experiments were performed by C.A.A.

Acknowledgments

This work was supported by grants-in-aid from the Ministry of Health, Labour, and Welfare of Japan (Health and Labour Sciences Research Grants, Research on Nanotechnical Medicine). This work was supported by a Research Grant for Cardiovascular Diseases

(18A-2) from the Ministry of Health, Labour, and Welfare of Japan, and Japan Association for the Advancement of Medical Equipment. The authors thank Jun-ichiro Enmi, Teramoto Noboru, Hajime Fukuda, and Akihide Yamamoto for their cooperation during this project.

Appendix. Supplementary material

Supplementary material associated with this article can be found, in the online version, at doi:10.1016/j.biomaterials.2011.11.075.

References

[1] Rafii S, Lyden D. Therapeutic stem and progenitor cell transplantation for organ vascularization and regeneration. Nat Med 2003;9:702–12.
[2] Kondo K, Shintani S, Shibata R, Murakami H, Murakami R, Imaizumi M, et al. Implantation of adipose-derived regenerative cell enhances ischemia induced angiogenesis. Arterioscler Thromb Vasc Biol 2009;29:61–6.
[3] Murohara T. Autologous adipose tissue as a new source of progenitor cells for therapeutic angiogenesis. J Cardiol 2009;53:155–63.
[4] Shintani S, Murohara T, Ikeda H, Ueno T, Sasaki K, Duan J, et al. Augmentation of postnatal neovascularization with autologous bone marrow transplantation. Circulation 2001;103:897–903.
[5] Hida N, Nishiyama N, Miyoshi S, Kira S, Segawa K, Uyama T, et al. Novel cardiac precursor-like cells from human menstrual blood-derived mesenchymal cells. Stem Cells 2008;26:1695–704.
[6] Iba O, Matsubara H, Nozawa Y, Fujiyama S, Amano K, Mori Y, et al. Angiogenesis by implantation of peripheral blood mononuclear cells and platelets into ischemic limbs. Circulation 2002;106:2019–25.
[7] Kocher AA, Schuster MD, Szabiolcs MJ, Takuma S, Burkhoff D, Wang J, et al. Neovascularization of ischemic myocardium by human bone marrow derived angioblast prevents cardiomyocyte apoptosis, reduces remodeling and improves cardiac function. Nat Med 2001;7:430–6.
[8] Leobon B, Roncalli J, Joffre C, Mazo M, Boisson M, Barreau C, et al. Adipose-derived cardiomyogenic cells: in vitro expantion and functional improvement in a mouse model of myocardial infarction. Cardiovasc Res 2009;83:757–67.
[9] Rafii S, Meeus S, Dias S, Hattori K, Heissig B, Shemelkov S, et al. Contribution of morrow-derived progenitors to vascular and cardiac regeneration. Cell Devl Biol 2002;13:61–7.
[10] Risau W. Mechanism of angiogenesis. Nature 1997;386:671–4.
[11] Folkman J, D'Amore PA. Blood vessel formation: what is its molecular basis? Cell 1996;87:1153–5.
[12] Asahara T, Masuda H, Takahashi T, Kalka C, Pastore C, Silver M, et al. Bone marrow origin of endothelial progenitor cells responsible for postnatal vasculogenesis in physiological and pathological neovascularization. Circ Res 1999;85:221–8.
[13] Shi Q, Rafii S, Wu MH, Wijelath ES, Cong Y, Ishida A, et al. Evidence for circulating bone marrow-derived endothelial cells. Blood 1998;92:362–7.
[14] Kalka C, Masuda H, Takahashi T, Gordon R, Tepper O, Gravereaux E, et al. Vascular endothelial growth factor$_{165}$ gene transfer augments circulating endothelial progenitor cells in human subjects. Circ Res 2000;86:1198–202.
[15] Asahara T, Murohara T, Sullivan A, Silver M, Zee RVD, Li T, et al. Isolation of putative progenitor endothelial cells for angiogenesis. Science 1997;274:964–7.
[16] Iwaguro H, Yamaguchi JI, Kalka C, Murasawa S, Masuda H, Hayashi SI, et al. Endothelial progenitor cell vascular endothelial growth factor gene transfer for vascular regeneration. Circulation 2002;105:732–8.
[17] Lyden D, Hattori K, Dias S, Costa C, Blaikie P, Butros L, et al. Impaired recruitment of bone-marrow-derived endothelial and hematopoietic precursor cells blocks tumor angiogenesis and growth. Nat Med 2001;7:1194–200.
[18] Kalka C, Masuda H, Takahashi T, Kalka-Moll WM, Silver M, Kearney M, et al. Transplantation of ex vivo explanted endothelial progenitor cells for therapeutic neovascularization. Proc Natl Acad Sci USA 2000;28:3422–7.
[19] Urbich C, Aicher A, Heeschen C, Dernbach E, Hofmann WK, Zeiher AM, et al. Soluble factors released by endothelial cells and cardiac resident progenitor cells. J Mol Cell Cardiol 2005;39:733–42.
[20] Urbich C, Dimmeler S. Endothelial progenitor cells characterization and role in vascular biology. Circ Res 2004;95:343–53.
[21] Urbich C, Heesechen C, Aicher A, Dernbach E, Zeiher AM, Dimmeler S. Relevance of monocytic features for neovascularization capacity of circulating endothelial progenitor cells. Circulation 2003;108:2511–6.
[22] Lewin M, Carlesso N, Tung CH, Tang TX, Cory D, Scadden DT, et al. Tat peptide-derivatized magnetic nanoparticles allow in vivo tracking and recovery of progenitor cells. Nat Biotechnol 2000;18:410–4.
[23] Wilhelm C, Bal L, Smirnov V, Galy-Fauroux I, Clement O, Gazeau F, et al. Magnetic control of vascular network formation with magnetically labeled endothelial progenitor cells. Biomaterials 2007;28:3797–806.
[24] Bulte JWM, Douglas T, Witwer B, Zhang SC, Strable E, Lewis BK, et al. Magnetodendrimers allow endosomal magnetic labeling and in vivo tracking of stem cells. Nat Biotechnol 2001;19:1141–7.
[25] Guzman R, Uchida N, Bliss TM, He D, Christopherson KK, Stellwagen D, et al. Long term monitoring of transplanted human neural stem cells in developmental and pathological contexts with MRI. Proc Natl Acad Sci USA 2007;104:10211–6.
[26] Hoehn M, Küstermann E, Blunk J, Wiedermann D, Trapp T, Wecker S, et al. Monitoring of implanted stem cell migration in vivo: a highly resolved in vivo magnetic resonance imaging investigation of experimental stroke in rat. Proc Natl Acad Sci USA 2002;25:16267–72.
[27] Amsalem Y, Mardor Y, Feinberg MS, Landa N, Miller L, Daniels D, et al. Iron-oxide labeling and outcome of transplanted mesenchymal stem cells in the infarcted myocardium. Circulation 2007;116:I.38–45.
[28] Terrovitis J, Stuber M, Youssef A, Preece S, Leppo M, Kizana E, et al. Magnetic resonance imaging overestimates ferumoxide-labeled stem cell survival after transplantation in the heart. Circulation 2008;117:1555–62.
[29] Li Z, Suzuki Y, Huang M, Cao F, Xie X, Connolly AJ, et al. Comparison of reporter gene and iron particle labeling for tracking fate of human embryonic stem cells and differentiated endothelial cells in living subjects. Stem Cells 2008;26:864–73.
[30] Winter EM, Hogers B, Van der Graaf LM, Gittenberger-de Groot AC, Poelmann R, Van der Weerd L. Cell tracking using iron oxide fails to distinguish dead from living transplanted cells in the infracted heart. Magn Reson Med 2010;63:817–21.
[31] Tachibana Y, Enmi JI, Mahara A, Iida H, Yamaoka T. Design and characterization of a polymeric MRI contrast agent based on PVA for in vivo living-cell tracking. Contrast Media Mol Imaging 2010;5:309–17.
[32] Yamaoka T, Tabata Y, Ikada Y. The fate of water-soluble polymers administered through different routes. J Pharm Sci 1995;84:349–54.
[33] Yamaoka T, Tabata Y, Ikada Y. Blood clearance and organ distribution of intravenously administered polystyrene microspheres of different sizes. J Bioact Compat Polym 1993;8:220–35.
[34] Yamaoka T, Tabata Y, Ikada Y. Body distribution profile of polysaccharides after intravenous administration. Drug Deliv 1993;1:75–82.
[35] Agudelo CA, Tachibana Y, Noboru T, Iida H, Yamaoka Y. Long-term in vivo magnetic resonance imaging tracking of endothelial progenitor cells transplanted in rat ischemic limbs and their angiogenic potential. Tissue Eng 2011;15-16:2079–89.
[36] Takahashi T, Kalka C, Masuda H, Chen D, Silver M, Kearney M, et al. Ischemia- and cytokine-induced mobilization of bone marrow- derived endothelial progenitor cells for neovascularization. Nat Med 1999;5:434–8.
[37] Takeshita S, Takaaki I, Mori H, Tanaka E, Eto K, Miyazawa Y, et al. Use of synchrotron radiation microangiography to assess development of small collateral arteries in a rat model of hindlimb ischemia. Circulation 1997;95:805–8.
[38] Ikenaga S, Hamano K, Nishida M, Kobayashi T, Li T, Kobayashi S, et al. Autologous bone marrow implantation induced angiogenesis and improved deteriorated exercise capacity in a rat ischemic hindlimb model. J Surg Res 2001;96:277–83.
[39] Marckmann P, Skov L, Rossen K, Dupont A, Damholt MB, Heaf JG, et al. Nephrogenic systemic fibrosis: suspected causative role of gadodiamide used for contrast-enhanced magnetic resonance imaging. J Am Soc Nephrol 2006;17:2359–62.
[40] Nissen NN, Polverini PJ, Koch AE, Volin MV, Gamelli RL, DiPietro LA. Vascular endothelial growth factor mediates angiogenic activity during the proliferative phase of wound healing. Am J Pathol 1998;152:1445–52.
[41] Daldrun-Link HE, Rudelius M, Metz S, Brauer R, Debus G, Corot C, et al. Migration of iron oxide labeled human hematopoietic progenitor cells in a mouse model: in vivo monitoring with 1.5-T MR imaging equipement. Radiol 2005;234:197–205.
[42] Caravan P, Ellison JJ, McMurry TJ, Lauffer RB. Gadolinium (III) chelates as MRI contrast agent: structure, dynamics, and applications. Chem Rev 1999;99:2293–352.

Ann Nucl Med (2012) 26:214–221
DOI 10.1007/s12149-011-0561-4

ORIGINAL ARTICLE

Monte Carlo simulation of scintillation photons for the design of a high-resolution SPECT detector dedicated to human brain

Yoshiyuki Hirano · Tsutomu Zeniya · Hidehiro Iida

Received: 15 June 2011 / Accepted: 23 November 2011 / Published online: 13 December 2011

Abstract
Objective In a typical single photon emission computed tomography (SPECT) system, intrinsic spatial resolution depends on the accuracy of the identification of an interacting point, which is dominated by propagation of the scintillation photons in the detector block. This study was intended to establish a Monte Carlo simulation-based evaluation tool taking into account the propagation of scintillation photons to estimate the intrinsic spatial and energy resolutions of the position-sensitive scintillator block in a SPECT detector.
Methods We employed Geant4 Monte Carlo simulation library which incorporated the optical photon processes for two different designs of the position-sensitive scintillator blocks. The validation of the simulation code was performed for a monolithic NaI(Tl) scintillator (251 × 147 × 6.4 mm^3) coupled to 15 flat-panel type multi-anode photo multiplier tubes (PMT) (H8500: Hamamatsu) and results were compared with those obtained experimentally. The code was then applied to a $LaBr_3$(Ce) scintillator of 120 mm square with varied thicknesses for designing high-resolution detector.
Results The simulation resulted in 2.6 mm full width at half maximum (FWHM) of spatial resolution and 9.0% FWHM of energy resolution for the NaI(Tl)-based detector, which were in a good agreement of the experimental results, i.e., 2.7 mm and 10%, respectively. These findings suggest that Geant4 simulation including optical photon processes enables to predict the spatial and energy resolutions of a SPECT detector block accurately. The simulation also demonstrated that 2 mm spatial resolution can be obtained for a 6 mm thickness of the $LaBr_3$(Ce), which is a significant improvement in performance as compared to existing gamma camera system that employs the scintillation detector fitted with PMTs.
Conclusions The Monte Carlo simulation-based evaluation tool was established to estimate the intrinsic spatial and energy resolutions of SPECT detector with position sensitive PMTs. This simulation may be useful to provide an optimal design of a SPECT detector without physical experiments.

Keywords $LaBr_3$(Ce) · Monte Carlo simulation · Geant4 · SPECT · Scintillation photon

Introduction

Single photon emission computed tomography (SPECT) is capable of providing tomographic images of radiolabeled tracers in vivo. The equipment essentially consists of position-sensitive detectors fitted with several types of collimators, which rotate around the object to be imaged. In most SPECT detectors, the point of interaction between a gamma ray and a scintillation crystal is identified by Anger logic on a 2-dimensional domain. Interacting coordinates are calculated by a weighted mean of the deposition of scintillation photons. Spatial resolution depends on the accuracy of identification, which may be degraded as a result of the propagation of scintillation photons within the detector system.

A Monte Carlo simulation is a helpful tool in designing a new detector block. The simulation code is often useful when optimizing design parameters of the detector block,

Y. Hirano (✉) · T. Zeniya · H. Iida
Department of Bio-medical Imaging,
National Cerebral and Cardiovascular Center Research Institute,
5-7-1 Fujishiro-dai, Suita, Osaka 565-8565, Japan
e-mail: hirano@ri.ncvc.go.jp

e.g., the thickness and other geometric parameters of the scintillator as well as the scintillator material, without the need for physical experiments. In order to estimate intrinsic spatial resolution and energy resolution, it is essential to understand the process of transport of scintillation photons in the detector system, as well as the interaction of gamma rays with materials. Geant4 [1] makes it possible to simulate both these processes. Simulation studies on propagation of scintillation photons have been performed using Geant4 (or other code) [2–6]. However, it is difficult to reproduce the intrinsic spatial and energy resolutions accurately due to the many unknown factors (e.g., optical properties of materials and electrical noise) to simulate transporting scintillation photons. Resolutions essentially depend on the number of obtained scintillation photons. Geant4 does not include the optical properties of materials, such as absorption length, refraction index, and reflection. These data must be entered into Gean4 by users. The simulation accuracy is sensitive to these optical parameters. To our knowledge, a validation study on spatial and energy resolutions using Geant4 was performed only by Van Der Laan et al. [2] for a positron emission tomography (PET) instrument that employed a monolithic scintillators (LYSO(Ce): 20 × 10 × 10 mm^3 and 20 × 10 × 20 mm^3) and avalanche photodiodes (APD).

In this work, we intended to use Geant4 for two types of position-sensitive scintillation detector in a SPECT system. Both detectors consist of a monolithic scintillator and flat-panel type multi-anode PMTs (H8500: Hamamatsu). These are different from detectors used in previous study [2] regarding scintillator material, detector size and photo-sensors. With regard to photo-sensor, detection principle of PMT is absolutely different from that of APD. One detector has a larger field-of-view (FOV) and is fitted with a parallel beam collimator for imaging the whole human brain. The detector block consists of a NaI(Tl) scintillator (251 × 147 × 6.4 mm^3) and 15 PMTs. Its experimental physical performance was used to validate the simulation code, including the photon propagation processes. We then extended this simulation geometry to another detector block, which consists of a $LaBr_3$(Ce) scintillator [7, 8] coupled to 4 PMTs to achieve higher intrinsic spatial resolution. This detector has smaller FOV and may be fitted with a pinhole collimator for focused imaging of a limited area of the brain with higher spatial resolution of approximately 1 mm [9]. We also investigated effects of inclined incident angle of gamma rays into the detector in a pinhole configuration on spatial resolution of the detector system.

Materials and methods

Monte Carlo simulation

We employed the Monte Carlo simulation library Geant4 (version 9.2.p02) in this study. Geant4 enables us to simulate not only interaction of gamma rays with several materials but also transport of scintillation photons. In this simulation, we took into account the following electromagnetic processes: Compton scatter, photo-electric effect, Rayleigh scatter, multiple scatter, bremsstrahlung, and ionization. The first three processes involve gamma rays; the rest involve electrons. Optical photon processes in the propagation of scintillation photons were also included: absorption, Rayleigh scatter, reflection, and refraction.

Simulations were carried out for essentially two sets of detector configurations as follows. The two sets of detector configurations (large-FOV detector and small-FOV detector) were precisely reproduced as shown in Fig. 1. The simulation configurations included scintillator, reflector, optical window, optical grease, PMT window, and PMT cathodes. Gamma rays entered the detector vertically,

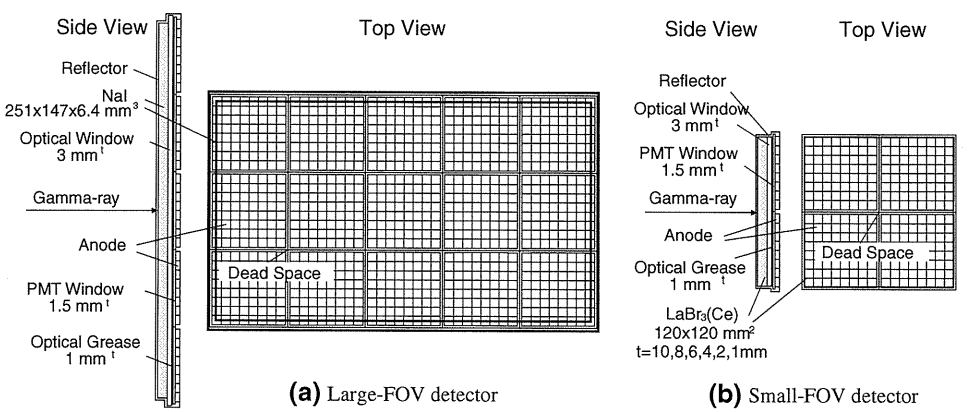

Fig. 1 Geometrical configurations of the large-FOV detector (**a**) and the small-FOV detector (**b**). In the simulation, we included the scintillator, reflector, optical window, optical grease, PMT window, and PMT anodes. The scintillator thickness of the small-FOV detector was varied (10, 8, 6, 4, 2, and 1 mm)

except for the simulation carried out for a pinhole configuration. When a gamma ray interacted with the scintillator and deposited its energy, scintillation photons were emitted isotropically. The emission spectra of NaI(Tl) and $LaBr_3$(Ce) are shown in Fig. 2a. The number of scintillation photons followed the Poisson distribution, and the mean was proportional to the energy deposition ($LaBr_3$(Ce): 63 photons/keV; NaI(Tl): 38 photons/keV). The scintillation photons propagated in the scintillator, optical window, optical grease and PMT window. At the reflector, the Lambert reflection was applied. The reflectance was 0.95 (white plastic). For a photon that was not reflected, propagation was terminated. At other boundaries between materials, the Fresnel reflection or Fresnel refraction was applied. When scintillation photon reached a cathode, the detection was determined by the quantum efficiency (Fig. 2a, gray line) and the collection efficiency (60%) of the H8500. The interacting point was reconstructed by Anger logic. An error of 17% was assigned to the anode gain. The error was estimated from anode uniformity map described in the specification. Transmittances of NaI(Tl) and borosilicate glass are shown in Fig. 2b. PMT cathodes and dead space surrounding the cathodes were assumed to be perfect absorbers. This simulation did not include absorptions by $LaBr_3$(Ce) and optical grease, because these transmittance data are not available. However, according to [10], the absorption for visible light is low. The thickness of optical grease was assumed as 1 mm. Refractive indices of, NaI(Tl), $LaBr_3$(Ce) and optical grease are 1.85, 1.9 and 1.465, respectively. With regard to borosilicate glass, the index was shown in Fig. 2c. These data were obtained from each specification.

Validation of the simulation code

To validate the Monte Carlo simulation, we compared spatial and energy resolutions obtained from the simulation with experimental values for the large-FOV detector. The experimental setup was as follows. The detector consisted of a monolithic NaI(Tl) scintillator (Saint-gobain) of 251 × 147 × 6.4 mm^3, fitted to 15 flat-panel type multi-anode PMTs (H8500: Hamamatsu) arranged in a 5 × 3 array. Each of the PMTs had 64 cathodes (8 × 8 array) that measured 5.8 mm square (6.08 mm pitch at center). The size of each PMT was 52 × 52 mm^2, and the PMT window was a 1.5 mm thickness of borosilicate glass that was transparent to visible lights. The NaI(Tl) scintillator was covered with a white diffuse reflector and an optical window of 3 mm thickness at the connection side of the PMTs. The optical window was also made of borosilicate glass. The NaI(Tl) scintillator was coupled to the PMTs by optical grease (BC630: Saint-gobain). Electric resistance arrays were connected to the anode outputs. The sum of the anode outputs and the positional coordinate (x, y) calculated by Anger logic were recorded in list mode. A specially designed collimator was placed in front of the detector block. The collimator was a 300 × 200 × 10 mm^3 block of lead with 170 holes of 1.5 mm diameter arranged in a 17 × 10 grid pattern with a grid interval of 15 mm. Small-tube sources (7 mm diameter) filled with Tc-99m solution were placed on 170 collimator holes, and position dependency of the energy spectra and point spread functions were measured. Energy and spatial resolutions were then evaluated.

In the simulation, spatial and energy resolutions were evaluated for the NaI(Tl)-based large-FOV detector by exposing 3000 gamma rays (141 keV) to the detector as a parallel beam with a circular distribution of 1.5 mm diameter at each of the hole positions. Interactions with the collimator were not included to reduce the computing time.

Application to the design of a new detector

Another series of simulations were carried out for the small-FOV detector to optimize the geometrical parameters. The scintillator was assumed to be $LaBr_3$(Ce) with a surface area of 120 × 120 mm^2. The scintillator was coupled to 4 PMTs (H8500) arranged in a 2 × 2 array. The

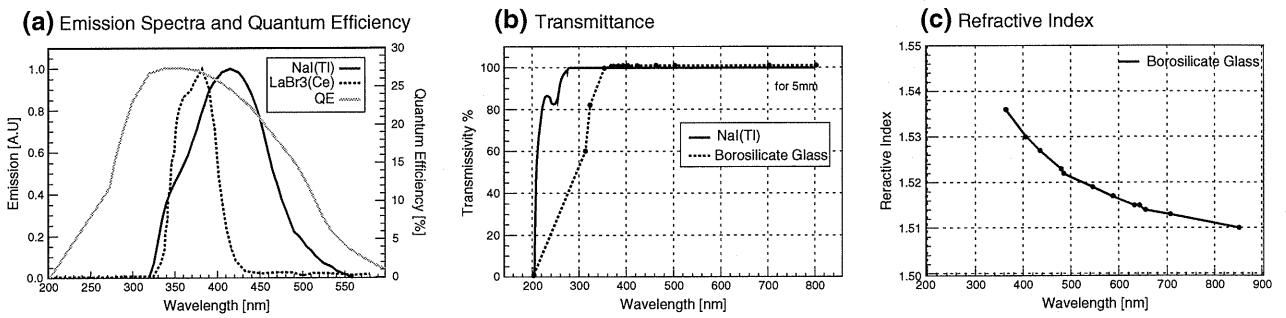

Fig. 2 **a** Emission spectra of NaI(Tl) (*solid line*) and $LaBr_3$(Ce) (*dotted line*) (BrilLanCe350: Saint-gobain) together with the quantum efficiency of the H8500 (*gray line*). **b** Transmittance of NaI(Tl) and borosilicate glass (assumed BK7: Schott Glass). **c** Refractive index of borosilicate glass. These data are available from each specification

surface of the scintillator was covered with a white diffuse reflector. The thickness of the scintillator was varied (10, 8, 6, 4, 2, and 1 mm) and the optical window thickness was also varied (1 and 3 mm). Simulation was also carried out using NaI(Tl) instead of $LaBr_3$(Ce) as the reference. Additional simulations were performed to evaluate effects of varying incident angle for a detector fitted with a pinhole collimator. Finally, detection efficiency defined as follows was estimated

$$\text{Efficency} = \frac{\text{Number of full energy despitions}}{\text{Number of incident gamma rays}}.$$

Densities of NaI(Tl) and $LaBr_3$(Ce) were 3.67 and 5.08 g/cm^3, respectively.

Gamma rays (141 keV) entered the scintillator vertically at 49 positions on a 7 × 7 grid with 15 mm intervals, similar to the source position of the large-FOV detector. In the pinhole configuration, gamma rays were generated at a point 86.6 mm above the center of the detector to the 49 positions. The maximum incident angle was 60°. 1000 gamma rays were simulated at each position.

Analysis

In both the simulation and experiment, the spatial and energy resolutions were evaluated at every grid points as follows. Photo-peak of 141 keV was fitted using a Gauss function, and 3-sigma region as an energy window (e.g., 116–164 keV for the experiment with NaI(Tl)) was selected. Using energy-selected events, interacting points were reconstructed by Anger logic and projected into the x and y directions. The spatial resolution was calculated by fitting with a function that took into account the diameter of holes, expressed as follows:

$$f(x) = \int g(x) \times h(z-x)\mathrm{d}x = \frac{1}{2a}\left\{\mathrm{erf}\left(\frac{a+b-x}{\sqrt{2}\sigma}\right) - \mathrm{erf}\left(\frac{b-x}{\sqrt{2}\sigma}\right)\right\},$$

$f(x)$ is assumed to be a convolution function of the Gauss function $g(x)$, which serves as a point spread function, and the uniform distribution $h(x)$, which describes the source distribution. erf is an error function, a is the diameter of a hole, and b is the position of a hole. The spatial resolutions for each position were calculated according to the term $\sqrt{8\ln 2} \times \sigma$, where σ is the standard deviation of the Gauss function. Finally, the energy resolution was derived from the energy spectra at each position. In this analysis of the experiment, background counts were subtracted from the experimental data.

We compared spatial resolution (FWHM mm) and energy resolution (FWHM %) with experimental results of the large-FOV detector. The planar image, spatial resolution in x and y direction, energy spectra, and their average resolutions were used for the comparisons. Finally, the small-FOV detector was designed to optimize spatial resolution and detection efficiency.

Results

Validation of simulation code

Planar images of multiple point sources obtained from the experiment and the simulation for the large-FOV detector are shown in Fig. 3. It can be seen that intervals between points are constant around the center, but becomes closer at the edge. The spatial resolution in the x direction along the central line is shown in Fig. 4. The spatial resolutions are almost homogenous around the center but become gradually worse at the edge of the detector in both the simulation and experiment. In the simulation, spatial resolution agreed with the experimental results within approximately 10% at ± 105 mm distance from the center. At the position 10 mm away from the detector edge, the resolutions become relatively worse. The experimental mean resolution, omitting those from the edge, were 3.6 and 3.1 mm in

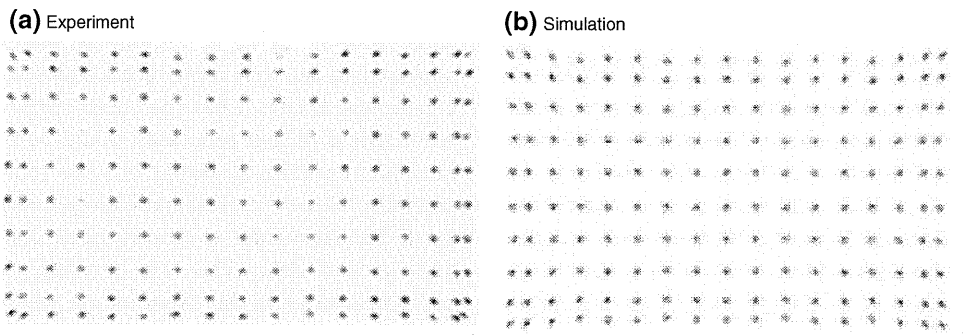

Fig. 3 Planar images of multiple point sources obtained from experiment (**a**) and simulation (**b**). These interacting points are calculated by Anger logic

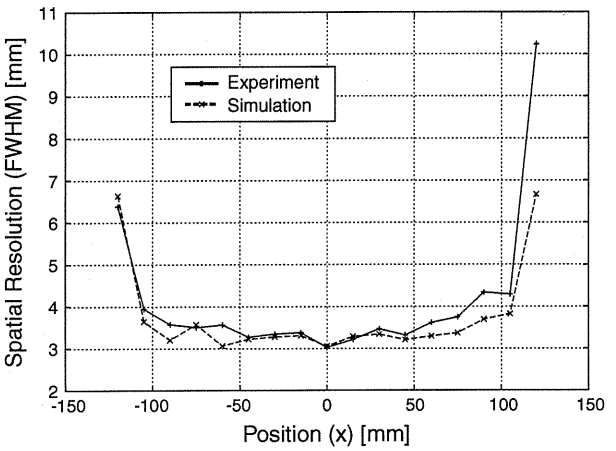

Fig. 4 Comparison of spatial resolutions in the x direction. The resolutions are for lines from the 5th row from the bottom in Fig. 3. The *solid line* shows the experimental result, and the *dotted line* shows the simulation result

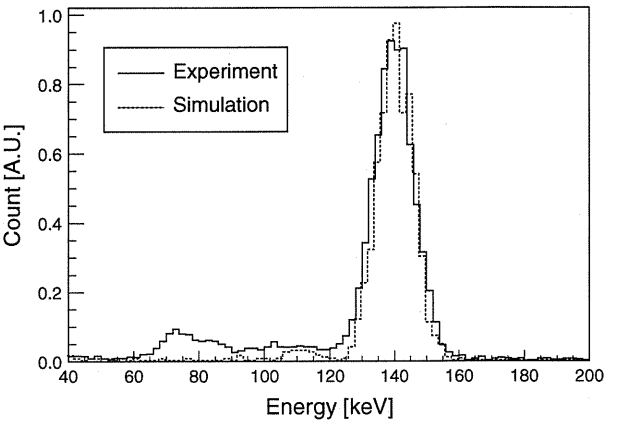

Fig. 5 Energy spectra at the center of the detector. The *solid line* shows experimental results; the *dotted line* shows the simulation. In the simulation, energy spectra are derived from the number of obtained scintillation photons

the x and y directions, respectively. The best resolutions in the x and y directions were 3.0 and 2.7 mm; these were obtained at the center. In the simulation, the mean resolutions in the x and y directions were 3.3 and 3.0 mm, respectively. The best resolutions were 2.8 and 2.6 mm for the x and y directions. Figure 5 shows the energy spectra at the center. The broadness of the peak in the simulation corresponds to the fluctuation of the number of obtained scintillation photons. The energy resolutions determined from spectra of the experiment and the simulation were 10.0 and 9.0% (FWHM), respectively. With respect to energy resolution, clear position dependence was not observed. The mean and deviation of energy resolution of the experiment and the simulation, respectively, were 10.3 ± 0.2 and 9.3 ± 0.3%.

Application of the simulation code for designing high-resolution detector

The simulation results of planar images of multiple point sources for the small-FOV detector with different thicknesses (10, 6 and 1 mm) are shown in Fig. 6. Clear separation of source positions was obtained in the thin scintillator, especially the 1 mm thickness. As the scintillator was thicker, interval of source positions decreased and the point spread function blurred. The mean spatial resolutions with thicknesses of 10, 8, 6, 4, 2, and 1 mm are shown in Fig. 7a together with the cases in which the scintillator is NaI(Tl), the thickness of the optical window is 1 or 3 mm, and the angle of incidence is oblique. In these configurations, comparable resolutions in the x and y directions were obtained. $LaBr_3$(Ce) had better spatial resolution than NaI(Tl) by 22–36%. The best resolution was 0.76 mm with 1 mm thickness. Energy spectra obtained from $LaBr_3$(Ce) and NaI(Tl) of 1 mm thickness at the center of the detector were shown in Fig. 8. The numbers of obtained scintillation photons in an event of full energy deposition (141 keV) were 5039 and 3103, resulting in energy resolution of 8.65 and 11.7%, respectively. The detection efficiencies are shown in Fig. 7b. The maximum efficiency for the 141 keV gamma rays was 93% with 10 mm thickness. The efficiency decreased with thinner scintillator (26% for 1 mm thickness). Varying the optical window between 1 and 3 mm had little effect. For the oblique incident cases, the spatial resolution became slightly worse by several percent.

Figure 9 shows an average distribution of scintillation photons on the 16 × 16 anodes in the case of 1000 gamma rays entering the of the detector. The thicker scintillator has a wider spread of scintillation photons.

Discussion

Adequacy of the simulation

This study demonstrates the adequacy of the simulation code. Both the spatial resolution and the energy resolution appeared to be well reproduced between simulation and experimental data. It has thus been suggested that Geant4 with optical photon processes would be of use when one intends to optimize the design of a new scintillation detector assembly. However, the simulation systematically exhibited small but significant overestimations compared with the experimental data. This can probably be attributed to additional errors in the experiments, which have not been taken into account in the simulation. Potentially influential factors include electrical noise and/or uncertainties in the multiplying processes of the PMTs. The angular

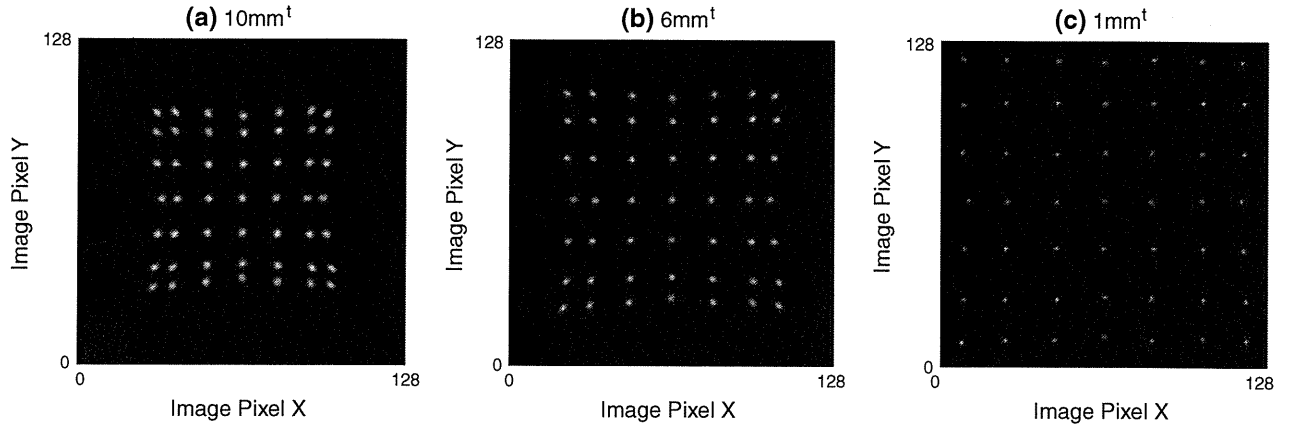

Fig. 6 Reconstruction of interacting points with a simulated $LaBr_3(Ce)$ scintillator with thickness 10 mm (**a**), 6 mm (**b**), or 1 mm (**c**). 141 keV gamma rays entered the $LaBr_3(Ce)$ scintillator vertically at 49 positions arranged in a 7 × 7 grid pattern with 15 mm intervals. Thinner scintillators have better spatial resolutions. Good separations and position linearity were obtained with a 1-mm thickness

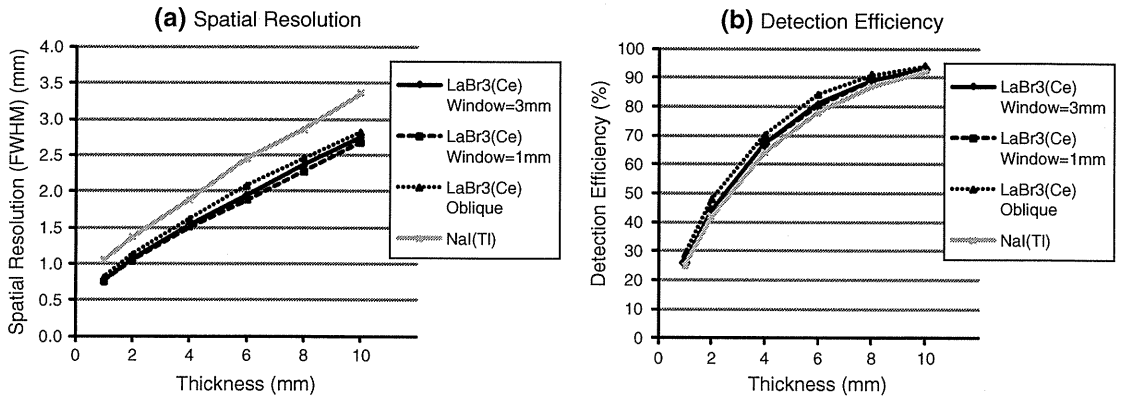

Fig. 7 Spatial resolutions (FWHM, mm) and detection efficiency (%) of the small-FOV detector estimated by simulation. Thickness was varied from 10 to 1 mm."OpWin" stands for the optical window. "Oblique" means that gamma rays enter the scintillator at an oblique angle

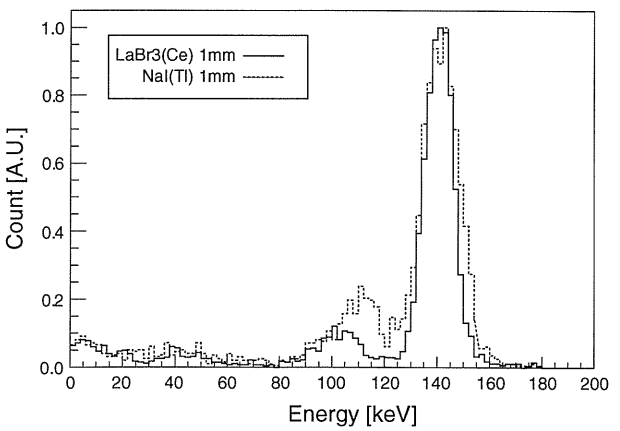

Fig. 8 Energy spectra $LaBr_3(Ce)$ (*solid line*) and NaI(Tl) (*dot line*) of 1 mm thickness at the center of the small FOV detector normalized by the maximum counts. Energy resolutions of $LaBr_3(Ce)$ and NaI(Tl) were 8.65 and 11.7%, respectively

distribution of the source is also considered as an influential factor. The beam was parallel in the simulation, but there were slight obliquely incidents in the experiment. Differences in the spatial resolution in the x and y directions can be attributed to difference of the number of cathodes along the x and y axes. The larger number of cathodes causes a larger uncertainty in the position identification due to the statistical fluctuation of scintillation photons at each anode. Note that the simulation of a square detector geometry for the small-FOV detector resulted in comparable resolutions for both the x and y directions. The spatial resolution has a position dependency, and decreases near the edge. This is because the distribution of the scintillation photons entering the cathodes is isotropic at the center, while scintillation photons partially reflect at the edge, resulting in an asymmetrical distribution at the edge of the detector. This caused decreased linearity performance and degraded spatial

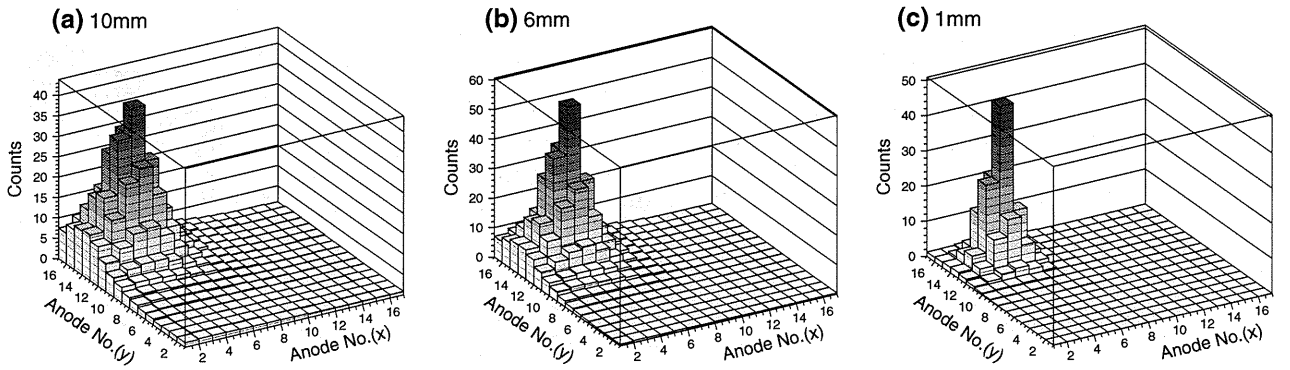

Fig. 9 Average distribution of scintillation photons on the 16 × 16 array of anodes. Gamma rays enter the edge of the detector. Scintillator thickness is 10 mm (**a**), 6 mm (**b**), or 1 mm (**c**)

resolution near the edge. Energy resolution depends on the number of observed scintillation photons. Homogeneous energy resolution indicates that the correction efficiencies of scintillation photons are almost equal over the entire detector. Importantly, the energy resolution was highly reproducible without any arbitrary parameters. It is often the case in most Monte Carlo simulation studies that energy resolution is fitted to match the experimental results. However, this simulation can reproduce the energy resolutions for a given set of detector design parameters. This is one of the most important features of this study. The simulated energy spectrum of the scatter region (below 120 keV) was different from the experimental results. It was probably due to the scatter from the collimator in the experiment. The simulation did not include interaction with the collimator.

Conceptual design of high-resolution SPECT system for human brain

We performed the simulation for optimizing a new high-resolution detector system for SPECT described in [9]. A pinhole collimator can be adopted to achieve the high spatial resolution typically achieved with a small-FOV. The reconstructed FOV can, however, be truncated if applied to an object which is larger than the FOV; this truncation can cause artifacts in the reconstructed images, and errors in the quantitative pixel counts. A new technique for truncation-compensated 3D-OSEM reconstruction [11], based on the theory proposed by Kudo et al. [12], could be one application of the two detectors presented in this study. One detector, with an NaI(Tl)-based large-FOV detector, provides an image without truncation, and is used as a supporting information for reconstructing truncated data from the small-FOV detector successfully. The small-FOV detector has the potential to provide high resolution of approximately 1 mm, but with possible truncation. Thus, the combination of the two types of detectors may provide SPECT images with both high spatial resolution and the quantitative accuracy of a magnified FOV. To achieve such a high resolution in practice, a prior high-accuracy estimate is essential. Monte Carlo simulation code, validated for a scintillator based on multi-anode PMTs, would be helpful for optimizing and validating various design configurations.

Design of the small-FOV detector with high resolution

$LaBr_3(Ce)$ is a promising material for use in scintillator crystals to achieve higher resolution than NaI(Tl); this is primarily due to the larger amount of scintillation photons, as demonstrated in this study. The thinner scintillator provides better spatial resolution, because thinner scintillators prevent the spread of scintillation photons, as shown in Figs. 6, 7 and 9. However, efficiency decreases with a thinner scintillator crystal, resulting in reduced sensitivity of gamma-ray detection. Thus, there is a trade-off between spatial resolution and detection efficiency. A thickness of 6 mm appeared to be best suited for our detector system, as we originally aimed at achieving a spatial resolution $\sim$1 mm with sufficient detection efficiency. If we use a pinhole collimator with 0.5 mm diameter and threefold magnification factor, an intrinsic spatial resolution of $\sim$2 mm would provide the spatial resolution of 1 mm in a SPECT system [13]. The simulation demonstrated that a 6 mm thickness of $LaBr_3(Ce)$ can provide $\sim$2 mm intrinsic spatial resolution and a detection efficiency of approximately 86% for Tc-99m, that efficiency is comparable to the performance of currently popular SPECT detectors. Using a pinhole collimator, spatial resolution could be slightly worse; this would be attributed to the spread of interaction points in the x–y plane due to the oblique angle of incidence. To evaluate the differences between vertical and oblique angles of incidence, it is necessary to simulate both gamma rays and scintillation photons, as we have done in this simulation study. Geant4 is of use for such evaluations, because it takes both processes into account.

Detector systems that consist of a monolithic scintillator and multi-anode PMTs have the potential to improve spatial resolution over what is currently achievable. In this study, Anger logic using all anodes was employed to identify an interacting point. Anger logic using a subset of anodes will improve the spatial resolution, the nearest-neighbor algorithm [14], and nonlinear least squares method [15] are also promising methods. In the future, in order to employ these methods, analog-to-digital converters (ADC) for all anodes will be installed in our detector systems.

Conclusion

We performed the Geant4 simulation that took into account propagation of gamma rays and transport of scintillation photons. The simulation reproduced experimental results with regard to both spatial resolution and energy resolution for a SPECT detector based on NaI(Tl) scintillator and position sensitive PMTs (H8500). We demonstrated a simulation for a design of the small-FOV detector to optimize geometrical parameter. This simulation may be useful to provide an optimal design of a SPECT detector without physical experiments.

Acknowledgments The authors would like to thank Mr. Hiroyuki Mashino of EspecTecno Corporation, Kobe, Japan, for his skillful assistance with an acquisition system of the detector. This work was supported in part by the Project from Kansai Bureau of Economy, Trade and Industry of Japan; a Grant for Research on Health Labour Sciences Research Grant, from the Ministry of Health, Labour and Welfare (MHLW) of Japan; the Budget for Nuclear Research of the Ministry of Education, Culture, Sports, Science and Technology (MEXT) of Japan; and the Grant-in-Aid for Scientific Research from MEXT of Japan.

References

1. Agostinelli S, Allison J, Amako K, Apostolakis J, Araujo H, Arce P, et al. GEANT4 a simulation toolkit. Nucl Instrum Methods Phys Res A. 2003;506:250–303.
2. Van Der Laan DJ, Dennis RS, Maas MC, Beekman FJ, Bruyndonckx P, van Eijk CWE. Optical simulation of monolithic scintillator detectors using GATE/GEANT4. Phys Med Biol. 2010;55:1659–75.
3. Sergio LM, Giuseppe B, Paolo B, Dante B, Valentino OC, et al. Optical physics of scintillation imagers by GEANT4 simulations. Nucl Instrum Methods Phys Res A. 2009;607:259–60.
4. Ciocia F, Braem A, Chesi E, Leo RD, Joram C, Lagamba L, et al. GEANT4 studies on the propagation and detection of scintillation light in long thin YAP crystals. Nucl Instrum Methods Phys Res A. 3009;600:506–12.
5. Wirth S, Metzger W, Pham-Gia K, Heismann BJ. Impact of photon transport properties on the detection efficiency of scintillator arrays. IEEE Nuclear Sci Symp Confer Record. 2006; 2602–3
6. Soreefan AM, Hui T, DeVol TA, Dept. Experimental and monte carlo investigation of the light collection efficiency of heterogenous scintillation flow cell detectors. IEEE Nuclear Sci Symp Confer Record. 2003;760–2
7. Pani R, Pellegrini R, Cinti MN, Bennatia P, Bettia M, Vittorinia F, et al. LaBr3:Ce crystal: the latest advance for scintillation cameras. Nucl Instrum Methods Phys Res A. 2007;572:268–9.
8. Pani R, Cinti MN, Pellegrinia R, Bennatia P, Bettia M, Vittorinia F, et al. LaBr3:Ce scintillation gamma camera prototype for X and gamma ray imaging. Nucl Instrum Methods Phys Res A. 2007;576:15–8.
9. Zeniya T, Hirano Y, Sakimoto T, Ishida K, Watabe H, Teramoto T, et al. Conceptual design of high resolution and a quantitative SPECT system for imaging a selected small ROI of human brain. IEEE Nuclear Sci Symp Confer Record. 2009; 3484–6
10. Li C, Wang B, Wang R, Wang H, Zhu Z. First-principles study of the electronic and optical properties of lanthanide bromide. Thin Solid Films. 2008;516:7894–8.
11. Zeniya T, Watabe H, Inomata T, Iida H, A Sohlberg, H Kudo. 3DOSEM reconstruction from truncated data in pinhole SPECT. IEEE Nuclear Sci Symp Confer Record. 2007; 4205–7
12. Kudo H, Courdurier M, Noo F, Defrise M. Tiny a prior knowledge solves the interior problem in computed tomography. Phys Med Biol. 2008;53:2207–31.
13. Jaszczak RJ, Li J, Wang H, Zalutsky MR, Coleman RE. Pinhole collimation for ultra-high-resolution small-field-of-view SPECT. Phys Med Biol. 1994;39:425–37.
14. Maas MC, Schaart DR, Van Der Laan DJ, Bruyndonckx P, Lemaitre C, Beekman FJ, et al. Monolithic scintillator PET detectors with intrinsic depth-of-interaction correction. Phys Med Biol. 2009;54:1893–908.
15. Zhi Li, Wedrowski M, Bruyndonckx P, Vandersteen G. Nonlinear least-squares modeling of 3D interaction position in a monolithic scintillator block. Phys Med Biol. 2010;55:6515–32.

Journal of Molecular Spectroscopy 274 (2012) 14–21

Contents lists available at SciVerse ScienceDirect

Journal of Molecular Spectroscopy

journal homepage: www.elsevier.com/locate/jms

Determination of two-photon-excitation cross section for molecular isotope separation

A. Wakai [a], K. Tsuchida [c], T. Fukumura [a,*], H. Iida [b], K. Suzuki [a]

[a] Department of Molecular Probes, Molecular Imaging Center, National Institute of Radiological Sciences, 4-9-1 Anagawa, Inage-ku, Chiba 263-8555, Japan
[b] Department of Bio-medical Imaging, National Cerebral and Cardiovascular Center Research Institute, 5-7-1 Fujishirodai, Suita-shi, Oosaka-fu 565-8565, Japan
[c] Medical System and Nuclear Equipment Division, Hitachi Works, Power Systems, Hitachi, Ltd., 1-1, Saiwai-cho, 3-chome, Hitachi-shi, Ibaraki-ken 317-8511, Japan

ARTICLE INFO

Article history:
Received 16 February 2012
Available online 28 March 2012

Keywords:
Elimination method
REMPI
C state
Molecular dissociation
A state
PET

ABSTRACT

We observed that the two-photon excitation of a υ_3 hot band (6*s* Rydberg $3;3_1^0$) in methyl iodide is promising for isotopic laser separation, because the isotope shift of the multiphoton ionization (MPI) resonance is resolvable. To estimate the excitation cross section, which gives the enrichment factor (final isotope ratio per initial isotope ratio) of the separation method, we devised a method based on a pump–probe MPI procedure. By probing the material remaining after irradiation with the pump pulse, we estimated the cross section of the ground-state transition (6*s* Rydberg 3;0–0) to be $4.1 \pm 1.4 \times 10^{-48}$ (cm^4 s). The enrichment factor predicted from this cross section indicates that a high-performance laser system (20 mJ/pulse, 200 Hz, 10 ns duration) was capable of achieving an enrichment of over 1000-fold in view of the dissociation efficiency under low-pressure gas conditions. Thus, laser separation (elimination) appears to be a promising tool to create positron-emission tomography molecular probes.

1. Introduction

An important theme in the use of positron-emission tomography (PET) has been to improve the specific activity (SA), which defined as the amount of radioactivity per unit mass of labeled compound [1]. Although ^{11}C-methyl iodide is a versatile precursor for ^{11}C-labeled molecular probes [2–4], it is contaminated during its synthesis by stable carbon isotopes, which reduces the SA [5–7] of the subsequent ^{11}C-labeled molecular probes. ^{11}C is usually diluted by three to four orders of magnitude below the level theoretically necessary. If a high-purity labeled compound could be obtained with the requisite SA, it would lead to a new and widespread use of PET technology [8]: for instance, to image new low-density receptors [9,10]. In working toward this goal, a chemical approach [10] obtained an order of magnitude (or more) increase in SA, but this corresponds to only 1/70 of the theoretically necessary level and appears to be close to the upper limit for the approach. Thus, a new approach is required.

Isotopic-enrichment techniques, especially UV laser separation [11,12] by isotopic molecular dissociation, can serve to increase the SA of labeled compounds, but they require an isotopically resolvable resonance. The two-photon excitation of the 6*s* Rydberg $3;3_1^0$ transition [13], which we found by resonance-enhanced multiphoton ionization (REMPI) of CH_3I to be isotopically resolvable [14], is a good candidate for UV separation. In what follows, we use the nomenclature of Felps et al. [15]. However, this transition is two-photon allowed and single-photon suppressed [13,16], and the cross section of two-photon excitation is extremely small in comparison with the cross section for single-photon excitation [17]. Thus, we focused our attention on studying the cross section of this excitation, which along with the laser characteristics, determines the performance of the laser separation method. However, no reports exist concerning this excitation cross section. In general, two-photon-excitation cross sections of molecules are measured by transmission methods such as Z-scan [18] techniques, two-photon-induced fluorescence [19,20], or ion-yield curve fitting based on rate equations [21]. However, these techniques are not suitable for CH_3I in low-pressure gas conditions because it dissociates without fluorescence from its excited state to fragments.

Therefore, we devised a method based on pump–probe multiphoton ionization (MPI) [22,23] and measured the excitation cross section of the relevant ground-state transition (6*s* Rydberg 3;0–0). Furthermore, we estimated the enrichment factor (final isotope ratio per initial isotope ratio) by a UV laser system from the obtained cross section. In the pump–probe MPI scheme, the probe normally selectively excites or ionizes either a product or the excited reactant, which is produced by the pump pulse. Examples of this approach include excited-state-dynamics studies [24], excited-state-lifetime measurements [25–27], fragment kinetics studies [28,29], or measurements of fragment population after dissociation [30]. However, in our method, the probe pulse is used to estimate

* Corresponding author. Fax: +81 43 206 3261.
E-mail address: t_fukumu@nirs.go.jp (T. Fukumura).

0022-2852/$ - see front matter © 2012 Elsevier Inc. All rights reserved.
http://dx.doi.org/10.1016/j.jms.2012.03.004

the amount of material remaining after irradiation by the pump pulse. Thus, the proposed method provides a direct estimation of the excitation cross section.

2. Experimental setup

The MPI system consisted of two laser systems: one for the pump beam and one for the probe beam, synchronized by a pulse generator (DG645, SRS), as indicated in Fig. 1. The second harmonic of a Ti:sapphire laser (LT-2211, LotisTII) pumped by the second harmonic of an Nd:YAG (532 nm) served as the pump beam. The pump pulse was centered at 370 nm, with a bandwidth of 0.1 nm, a 10 ns full-width at half-maximum (FWHM), a repetition rate of 7 Hz, and pulse energy of 3.1 mJ. The laser beam was linearly polarized parallel to the electric field formed between the repeller (2.1 kV/cm) and the ground plate, which had a grid in the center to permit the flow of ions through the detector (see Fig. 1).

The probe beam consisted of the forth harmonic of a Nd:YAG laser (LT-2134UTF, LotisTII). The probe pulse was centered at 266 nm, with an FWHM of 5–6 ns, a 7 Hz repetition rate, and pulse energy of 0.21 mJ. The pulse beam was linearly polarized perpendicular to the electric field between the repeller and ground plate and arrived at the sample with an 80 ns delay with respect to the pump pulse.

The laser beams were spatially overlapped and focused into the ionization chamber by a fused-silica lens (focal length 300 mm). The spot size at the focal point of the pump beam was measured by a profile monitor (BC103, Ophir Optronics Ltd.), which yielded a $1/e$ radius at the beam waist of 73 μm (see Fig. 2). It was not possible to measure the probe beam with the profile monitor because its wavelength (266 nm) was beyond the range of the profile monitor. However, our time-of-flight (TOF) system is sensitive to position; hence, by comparing the 8-ns FWHM TOF distribution of iodine ions generated by the pump pulse to the 7-ns FWHM TOF distribution of iodine ions generated by the probe pulse, we estimated the radius of the probe-beam waist to be 59 μm.

To ensure the spatial overlap of the pump and probe beams at the sample position, we simultaneously observed MPI signals from the two pulses. To optimize the horizontal beam position, we adjusted the horizontal angle of the high-reflection (HR) guide mirror (see Fig. 1) while monitoring the TOF distributions by the oscilloscope. To optimize the vertical beam position, we adjusted the vertical angle of the HR mirror so as to minimize the number of parent ions generated by the pump pulse.

To change between pump–probe and probe-only mode, we used mechanical shutters, as shown in Fig. 1.

Ions produced by MPI were directed by a 2.1 kV/cm electric field into a 10 cm TOF tube, at the end of which, they were detected by a microchannel plate (MCP; F4655-10, Hamamatsu Photonics). The signals were transformed by a pump-triggered oscilloscope into TOF distributions, and averaged over 512 events were stored.

The sample material CH_3I (Wako Pure Chemical Industries, Ltd.) was kept in a glass cell cooled to the temperature of ice water. The vapor flow rate (0.19 atm. at 0 °C) into the vacuum chamber was controlled by a mass flow controller (M200S-TE07037, MKS). During MPI experiments, the CH_3I vapor pressure in the chamber was monitored by an ion gauge and maintained at approximately 1.3×10^{-4} Pa.

3. Principle of estimation

3.1. Enrichment factor

The sample vapor was contained in a glass cell and irradiated by UV laser pulses at frequent ~140 ms intervals. To achieve laser separation, we use the elimination method [31,32]. The pump pulse wavelength is tuned to excite the isotopic counterpart molecule ($^{12}CH_3I$) rather than the molecule of interest ($^{11}CH_3I$). The excited molecule then fragments, and the fragments are eliminated chemically. The number of counterpart molecules [$N_{12}(t)$] obeys the rate equation

$$-\frac{d}{dt}N_{12}(t) = \eta \cdot N_{12}(t), \tag{1}$$

where η is the dissociation rate (s^{-1}). The solution to Eq. (1) is

$$N_{12}(t) = N_{12}(t=0) \cdot \exp(-\eta \cdot t). \tag{2}$$

In the present case, the dissociation rate of ground-state CH_3I approximately corresponds to the excitation rate because the inverse lifetime of the excited state that follows dissociation is

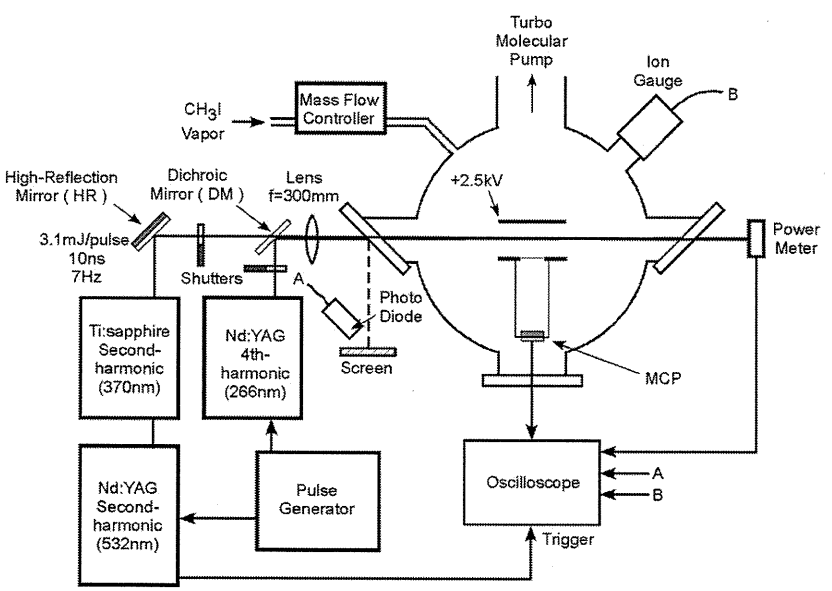

Fig. 1. Schematic of experimental apparatus, showing pulsed laser systems, system to synchronization pump and probe pulses, and the ion-detection system.

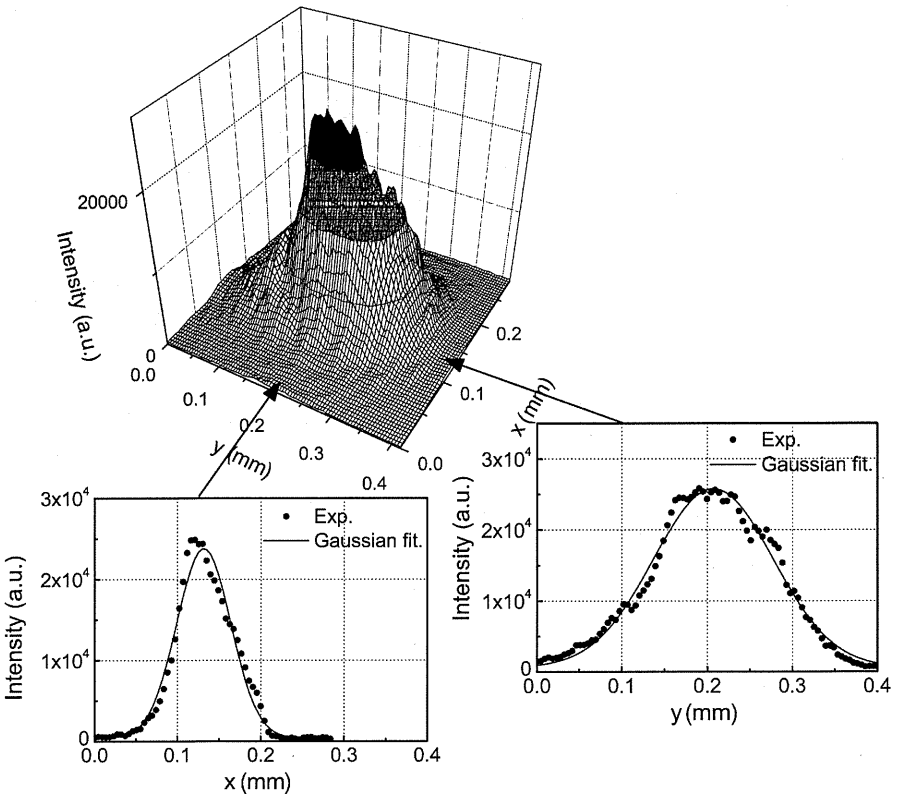

Fig. 2. Spatial profile of the pump pulse (370 nm) at the focal point. The beam focus elliptical. The $1/e$ radius of the profile was estimated to be 73 μm by averaging the y radius (major axis, 100 μm) and the x radius (minor axis, 45 μm).

significantly greater than the expected laser excitation rate (see Appendix A). Considering the laser reaction volume V into the cell volume V_C leads to the following dissociation rate:

$$\eta = \frac{V}{V_C}\sigma I, \tag{3}$$

where σ is the excitation cross section and I is the peak photon density delivered by the laser pump pulse ($cm^{-2}\,s^{-1}$). Using the number of dissociated molecules per pulse, the molecule density can be described by

$$N_{12}(n) = N_{12}(0)\exp\left(-\frac{V}{V_C}\sigma I\Delta t n\right). \tag{4}$$

For two-photon excitation, using the effective volume $V^{(2)}$ and the effective duration $\tau^{(2)}$ of pump pulse (see Appendix B), the number of the molecules can be described by

$$N_{12}(n) = N_{12}(0)\exp\left(-\frac{V^{(2)}}{V_C}\sigma^{(2)}I^2\tau^{(2)}n\right). \tag{5}$$

Using Eq. (5), the enrichment factor is given by [33,34]

$$\beta = \frac{N_{11}(n)/N_{12}(n)}{N_{11}(0)/N_{12}(0)} = \exp\left(\frac{V^{(2)}}{V_C}\sigma^{(2)}I^2\tau^{(2)}n\right), \tag{6}$$

assuming that $N_{11}(n) = N_{11}(0)$. Using Eqs. (B.9) and (C.1), the enrichment factor is

$$\beta = \exp\left(\frac{1}{2\sqrt{2}}\frac{V}{V_C}\sigma^{(2)}I^2\Delta t n\right). \tag{7}$$

For our purpose (i.e., CH_3I isotopic enrichment), we use the transition from the ν_3 vibronic state of the electronic ground state to the 6s Rydberg [3] state, which we call the "hot band" excitation (or the R 6s $3;3_1^0$ transition). That is, our target is the vibronic excited state of the molecule. Therefore, the number of real target molecules depends on the population of the ν_3 vibronic excited state. Considering the population ($b = 0.076$) of the ν_3 vibronic excited state at room temperature [35], the enrichment factor takes the form

$$\beta = \exp\left(\frac{1}{2\sqrt{2}}\frac{V}{V_C}b\sigma_{ex}^{(2)}(\nu_3)I^2\Delta t n\right) \tag{8}$$

where $\sigma_{ex}^{(2)}(\nu_3)$ is the two-photon-excitation of the hot band. This cross section is described in terms of the cross section $\sigma_{ex}^{(2)}$ of the transition from the electronic and vibronic ground states to the 6s Rydberg [3] state, (that is R 6s 3;0–0); $\sigma_{ex}^{(2)}$, as follows:

$$\sigma_{ex}^{(2)}(\nu_3) = f_{FC}\sigma_{ex}^{(2)}, \tag{9}$$

where f_{FC} is the Franck–Condon (FC) factor [36], which represents the overlap between the vibronic ground-state wavefunction and the ν_3 vibronic excited state wavefunction (single vibrational quantum). Substituting Eq. (9) in Eq. (8), the enrichment factor becomes

$$\beta = \exp\left(\frac{1}{2\sqrt{2}}\frac{V}{V_C}bf_{FC}\sigma_{ex}^{(2)}I^2\Delta t n\right) \tag{10}$$

In deriving Eq. (10), we assumed that the cell length in the beam direction is significantly less than the laser-beam focal length. Thus, the volume ratio approximately corresponds to the ratio of the cell window area to the cross-sectional area of the laser-beam waist, which we take as 1/4 in the present study. Therefore, for the laser to penetrate into the cell without distorting the laser profile, the radius of the cell window must be at least two times the radius of the beam.

It is apparent from Eq. (10) that accurately measuring the excitation cross section is essential to obtain a good estimate of the

enrichment factor. The photon density I and the laser pump pulse duration Δt depend on the laser system used.

Although we intended to measure the cross section of the hot band transition, the pulse power of our current laser system was insufficient to detect any dissociation effect based on the hot band transition. Therefore, we estimated the excitation cross section of the dominant ground-state transition, whose cross section is related to the cross section of the hot band transition by Eq. (9).

3.2. Signal reduction ratio

Fig. 3 shows an energy-level diagram of the ionization of methyl iodide CH_3I. The 370-nm pump-pulse wavelength yields parent and fragment ions from (2 + 1) REMPI via the 6s Rydberg [3] state, as shown in Fig. 3a. Actually, most excited molecules (>99.8%) dissociate into fragments (methyl radical and the excited iodine atom) within the pulse width Δt of our (pump and probe) laser pulses. The 266-nm probe pulse wavelength excites ground-state molecules to state A, which dissociate within 100 fs to neutral fragments [37], as shown in Fig. 3b. Subsequently, the fragments (CH_3 and I) are ionized by the same probe pulse [38,39].

The probe pulse probed the volume irradiated by the pump pulse, but with an 80 ns delay time, as indicated in Fig. 4. First, the pump pulse dissociates the CH_3I molecules within the volume V_U, which causes the molecular density within this volume to decrease. The density of the remaining molecules is monitored by the ion signals obtained from the probe pulse. The excitation cross section is obtained from the difference in the ion yields by the probe pulse with and without the pump (i.e., $\Delta Q = Q_{\text{pump on}} - Q_{\text{pump off}}$, where Q is the ion yield of the probe pulse).

In our experimental setup, the laser beam was focused at the cell by a convex lens to produce MPI within the sample. Thus, sample molecules within the laser-beam focal volume were ionized. Among the ions produced in this focal volume, only those within the beam axis length L_z corresponding to the detector diameter were detectable. Therefore, we considered the laser spatial distribution to be transverse Gaussian [$P(r/w)$, where w is the $1/e$ beam radius] and longitudinally uniform, as descried in Appendix B. In this case, by Eq. (B.7), the ion yields Q_B for the pump-off case are described by

$$Q_B = \rho \varepsilon_B^{(4)} I_B^4 \int P^4\left(\frac{r}{w_B}\right) 2\pi r dr L_z \tau_B^{(4)}, \tag{11}$$

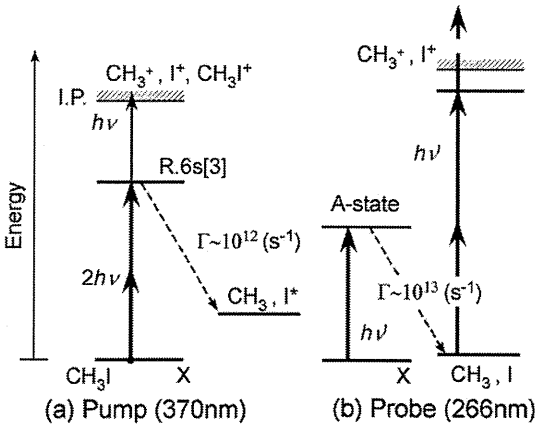

Fig. 3. Energy-level diagrams of CH_3I showing resonance levels relevant to the fragment- and parent-ion yields. (a) (2 + 1) REMPI via the R 6s [3] state, molecules excited to this state mainly dissociate to a neutral fragment, a methyl radical, and an excited iodine atom with a dissociation rate Γ. (b) MPI via state A. The fragments (methyl radical and iodine atom) dissociated from state A (lifetime ~100 fs [37]) are ionized by multiphoton absorption.

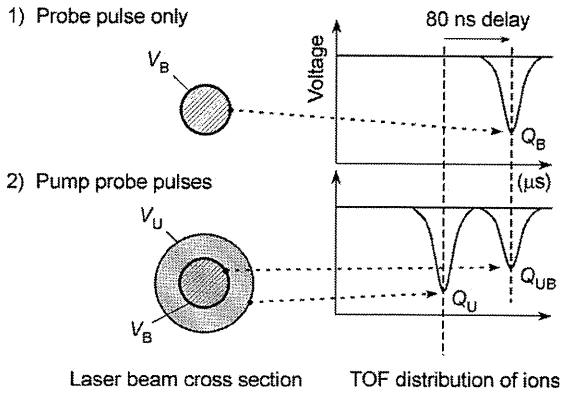

Fig. 4. Scheme to estimate the excitation cross section. The density of the target material decreases upon excitation by the pump pulse and subsequent dissociation. The decreased density leads to a reduction in probe-pulse ionization. V_U and V_B represent the reaction volumes of the pump and probe pulses, respectively.

and the ion yields Q_{UB} for the pump-on case are described by

$$Q_{UB} = \rho \varepsilon_B^{(4)} I_B^4 \int \left[1 - \sigma_{ex}^{(2)} I_U^2 P^2\left(\frac{r}{w_U}\right) \tau_U^{(2)}\right] P^4\left(\frac{r}{w_B}\right) 2\pi r dr L_z \tau_B^{(4)}, \tag{12}$$

where $\varepsilon_B^{(4)}$ is the ionization cross section of the probe pulse, and the subscripts U and B refer to the pump pulse and probe pulse, respectively. From Eqs. (11) and (12), the reduction ratio of the ion yields is

$$\frac{Q_{UB}}{Q_B} = 1 - \sigma_{ex}^{(2)} I_U^2 \tau_U^{(2)} \left(\frac{\int P^2\left(\frac{r}{w_U}\right) P^4\left(\frac{r}{w_B}\right) 2\pi r dr}{\int P^4\left(\frac{r}{w_B}\right) 2\pi r dr} \right). \tag{13}$$

Therefore, the reduction ratio of ion yields is given by

$$\frac{Q_{UB}}{Q_B} = 1 - \frac{\sigma_{ex}^{(2)} I_U^2 \tau_U^{(2)}}{\frac{S_B}{2S_U} + 1}, \tag{14}$$

where $S_U (= \pi w_U^2)$ and $S_B (= \pi w_B^2)$ are the cross-sectional areas of the laser-beam waist for the pump and probe beams, respectively. If we define the reduction ratio of the ion signal as

$$R_{rd} = \frac{Q_{UB}}{Q_B}, \tag{15}$$

the excitation cross section may be expressed as

$$\sigma_{ex}^{(2)} = \frac{1}{I_U^2 \tau_U^{(2)}} \left(\frac{S_B}{2S_U} + 1\right)(1 - R_{rs}). \tag{16}$$

Replacing the effective pump-pulse time $\tau_U^{(2)}$ with the actual time (Δt_U) by Eq. (C.1) gives

$$\sigma_{ex}^{(2)} = \frac{\sqrt{2}}{I_U^2 \Delta t_U} \left(\frac{S_B}{2S_U} + 1\right)(1 - R_{rd}). \tag{17}$$

We experimentally obtained the reduction ratio R_{rd} and used Eqs. (10) and (17) to estimate the enrichment factor.

Note that our method assumes that the fragments are not ionized by the probe pulse. We assume that the iodine atom that dissociates from the 6s Rydberg [3] state is excited to $I^*(^2P_{1/2})$ [40]. Unlike ground-state iodine, iodine in this excited state does not have a transition that is resonant with the probe-pulse photon energy. Detection of I^+ is suitable for our method. However, although the methyl radical is ionized by the probe pulse, it is released from the reaction volume with the kinetic energy of molecular dissociation. During the pump–probe delay time (80 ns), the methyl radical with a velocity of 4×10^3 m/s [41] travels approximately 0.32 mm, which is greater than the radius of the probe-beam waist. Therefore, most of the radicals are not irradiated by the probe pulse.

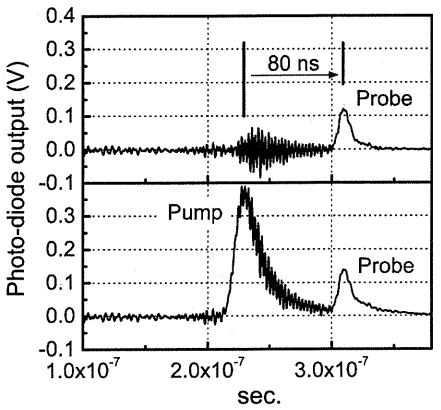

Fig. 5. Timing of two laser pulses using a photodiode detector. The probe pulse arrives at the sample 80 ns after the peak of the pump pulse. The ringing noise in the upper panel is attributed to the electrical noise caused by the flash pumping of the Nd:YAG gain medium in the probe laser. Because this noise disappeared when we stopped the Nd:YAG laser (probe pulse).

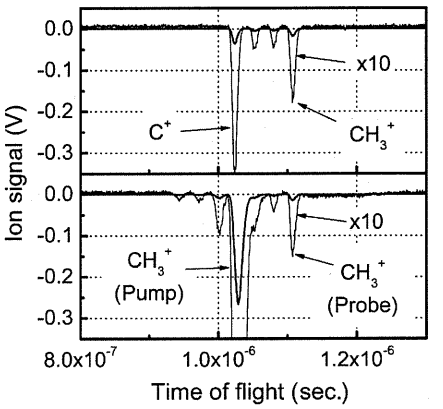

Fig. 6. Time-of-flight distributions of methyl radical ions generated solely by the probe pulse (upper panel) and by the pump and probe pulses (lower panel).

However, out of concern that the ionization of methyl radical fragments having flight paths parallel to the laser axis would distort the signal, we did not use data from the methyl radical ions to estimate the requisite cross section.

4. Results

The timing between the pump and probe pulses was monitored by a photodiode for both probe-only (Fig. 5, top panel) and pump–probe modes (Fig. 5, bottom panel). The pulse generator output reveals that the probe pulse followed the pump pulse. A ringing noise appeared before the probe pulse, but this noise disappeared when we stopped the Nd:YAG laser (i.e., the probe beam laser). Therefore, we attribute the noise to electrical noise generated by the flash pumping of the Nd:YAG laser gain material. Because of the insufficient bandwidth of our photodiode (cutoff frequency = 900 MHz), we consider that the actual width of the pump pulse is less than the 26 ns measured with our photodiode.

Fig. 6 shows the TOF distributions of the fragment ions (methyl radical ions). The upper panel shows results for the probe-only mode. The four peaks correspond to CH_n^+ ($n = 0, 1, 2, 3$). The last one of the four peaks corresponds to the methyl radical ion (CH_3^+). The lower panel shows results of the pump–probe mode. The largest peak in the lower panel corresponds to methyl radical ions (CH_3^+) generated by the pump pulse. The C^+ peak that appears in the upper panel overlaps temporally with the CH_3^+ peak generated by the pump pulse (lower panel). The methyl radical ion signal in the lower panel appears to be slightly smaller than that in the upper panel. From the magnitudes of these peaks, we estimated the reduction ratio of the methyl radical ions.

Fig. 7 shows the TOF distributions of iodine ions (I^+) and parent ions (CH_3I^+). The largest of the three peaks in the lower panel corresponds to iodine ions generated by the pump pulse, and the center of the three peaks corresponds to I^+ generated by the probe pulse. We can see that the I^+ peak in the lower panel (pump probe) is smaller than that in the upper panel (probe only). We attribute the decrease in the I^+ peak to the dissociation of methyl iodide molecules caused by the pump pulse. We estimate the reduction ratio of I^+ from the magnitude of these peaks.

The reduction ratios of the signals of the fragment ions (CH_3^+ and I^+) due to the probe pulse were calculated using Eq. (15) and are shown in Fig. 8. We observe a significant reduction of probe-generated ions, which we attribute to the depletion of the parent population caused by the pump pulse. The errors shown in the

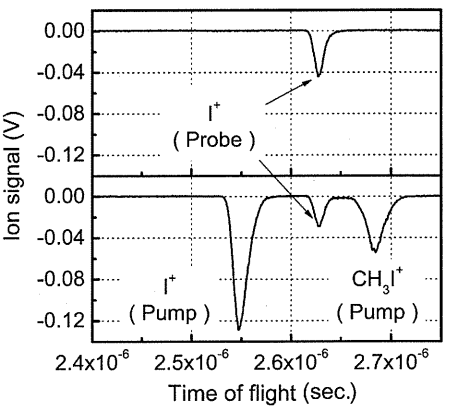

Fig. 7. Time-of-flight distributions of iodine ions and parent molecules generated by the probe pulse alone (upper panel) and by the pump and probe pulses (lower panel).

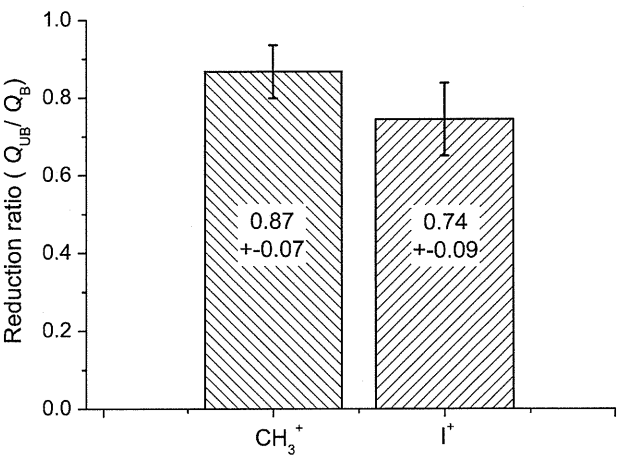

Fig. 8. Reduction ratio for ions fragmented by the probe pulse after irradiation by the pump pulse.

figure represent the standard deviation of our data (8 samples). To estimate the excitation cross section at the pump wavelength, we used the reduction ratio of 0.74 ± 0.09 for I^+. Then, by Eq. (17), we obtained the two-photon-excitation cross section of the R 6*s* 3;0–0 transition as $4.1 \pm 1.4 \times 10^{-48}$ (cm^4 s).

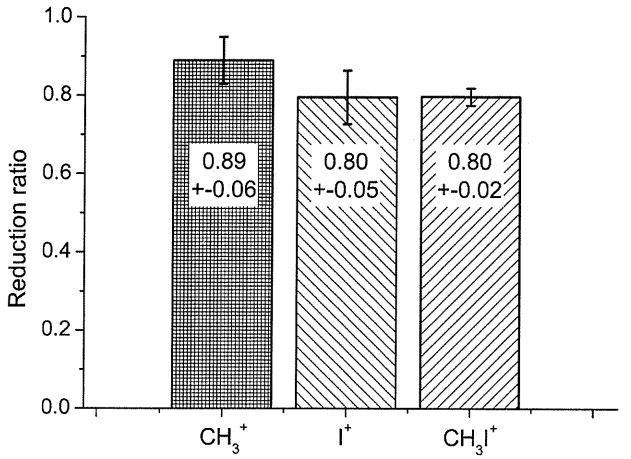

Fig. 9. Reduction ratio for fragment and parent ions generated by the probe pulse (370 nm) after irradiation by the pump pulse (266 nm).

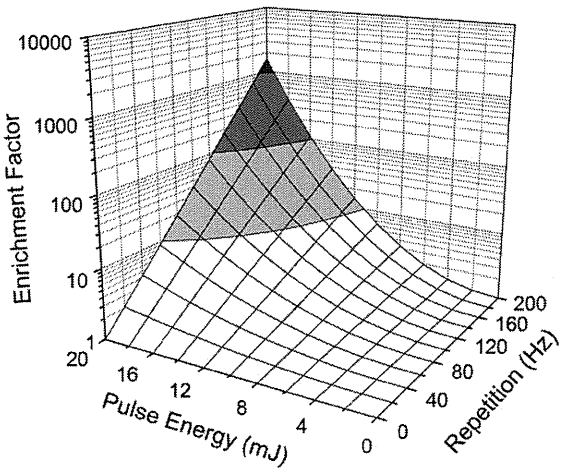

Fig. 10. Predicted enrichment factor for $[^{11}C]CH_3I$ estimated using the lower case of the experimentally estimated cross section (2.7×10^{-48} cm^4 s: see Eq. (10)). Parameters were beam-waist radius = 0.375 mm, optical cell radius = 0.75 mm, enrichment time = 20 min, pump-pulse duration = 10 ns. This calculation does not consider material loss by the decay of ^{11}C.

To evaluate the reliability of our method, we compared the number of ions estimated from the signal intensity per pulse with that estimated from the two-photon cross section obtained using the rate equation. We calculated the number of ions detected per pulse by our TOF system to be approximately 68 using the single-ion signal height (23 mV) from our MCP detector, considering the permeation ratio of the grid in our TOF system of 0.73 and the MCP open-area ratio [42] of 0.6. From the rate equation, we obtained the ion yield of 9–900 (Appendix A) using the effective reaction volume (Appendix B) and the effective duration (Appendix C). This range includes the result (approximately 68) from the TOF signals. Thus, the result for the ion yield is likely to prove acceptable to estimate two-photon-excitation cross sections.

In addition, we obtained the cross section for a single-photon excitation to state A and measured the ion yields for the probe-only and pump–probe modes. For these measurements, we used 266-nm pump pulses and 370-nm probe pulses with the same (80 ns) delay time between the pump and probe. The reduction ratios of the fragment and parent ions are shown in Fig. 9. We calculated the reduction ratio of the parent ion to be 0.80 ± 0.02 and the resulting excitation cross section to be $1.2 \pm 0.1 \times 10^{-19}$ cm^{-2}. Rattigan et al. [43] reported an absorption cross section for state A to be 9×10^{-19} cm^{-2}, which is about an order of magnitude larger than our result. This discrepancy is not surprising because the single-photon absorption cross section will include the effects of Raman scattering and absorption by fragment excited states, but Rattigan et al. did not include the error associated with their result. Another reason for this discrepancy might be related to the difference in sample environment within the reaction volume. Our material was exposed to an electric field for ion extraction. Considering the errors in the cross section (which are discussed in the next section) and the effects of the different environments, we consider this discrepancy to be reasonable.

From the lower case of the estimated two-photon cross section [$(4.1-1.4 = 2.7) \times 10^{-48}$ cm^4 s], we calculated the enrichment factors for $[^{11}C]CH_3I$ [Eq.(10), see Fig. 10] as a function of both pump-pulse energy and repetition rate. For this calculation, we assumed the FC factor to be 0.24, which was calculated from the R 6*p* $4;3_0^1$ transition MPI [44] and the relevant origin-band excitation signal instead of the R 6*s* $3;3_1^0$ transition. We selected this transition because this MPI scheme is unlikely to suffer from autoionization [45], and the peak MPI signal for this transition does not overlap other resonance peaks. In addition, we assumed a beam-waist radius for an enrichment of 0.375 mm, an optical-cell radius (a capillary-like cell) of 0.75 mm, and an enrichment time of 20 min, which is the half life of ^{11}C. The pulse duration was considered to be 10 ns. For pulse energy and repetition rate, we used the specifications of typical commercial dye laser systems. The results shown in Fig. 10 indicate that a high-performance laser system with a pulse power of 20 mJ and a repetition rate of 200 Hz is capable of enriching carbon-substituted methyl iodide by approximately 1700-fold. In this case, the SA of the present methyl iodide agent would be increased to the theoretically required level.

5. Discussion

We measured the two-photon-excitation cross section of the R 6*s* 3;0–0 band of CH_3I based on our pump–probe MPI experiment. From the cross section obtained for the transition from the ground state to the R 6*s* 3;0–0 state, we calculated the enrichment factor achieved by laser separation via the hot band transition. Based on the dissociation efficiency and assuming high-performance lasers are used, we find that laser separation based on the hot band transition would be practical to enrich $[^{11}C]CH_3I$ up to theoretically required SA levels. Thus, the laser separation technique seems promising for the synthesis of ^{11}C-labeld compounds use with PET radiopharmaceuticals.

However, our estimate of the high SA attainable by the proposed method includes limits to precision that result from several assumptions and experimental ambiguities. Three sources of error are included in the estimate of the cross section: (1) the misalignment of the two laser axes; (2) the thermal velocity of molecules; and (3) the effect of condensed gas (vapor).

The effect of misaligning laser beams on two-photon absorption processes has been studied by Swofford and McClain [46], who showed that a 12% signal loss occurs for a misalignment of half the radius of a Gaussian beam. In the present study, we assumed a maximum misalignment of half the radius of the laser-beam waist. If this maximum misalignment proved real, the reduction ratio obtained would be reduced by 12%; in other words, the actual cross section would increased by 13%.

The thermal velocity of the sample molecules affects the measurements because the molecules travel at this velocity during the pump–probe delay time. At room temperature, the CH_3I molecule has a root-mean square speed of 230 m/s, and hence can travel approximately 0.02 mm during the pump–probe delay time, which

is less than the diameter of the effective volume. Thus, this effect does not significantly affect the estimate of the two-photon cross section. However, by the 300 K Maxwell–Boltzmann velocity distribution, we calculated that 8% of the molecules in the reaction volume exchange with outside molecules during the pump–probe delay time. Incorporating these exchanged molecules in our calculation results in a maximum 9% increase in the two-photon cross section. From previous discussions, the two-photon cross section of the ground state transition might increase to a maximum of 21%. Such increases in the two-photon cross section would lead to an increase in the enrichment factor.

After dissociation of CH_3I in the gas phase, neutral fragments (methyl radicals and excited iodide) dissociated from the excited state can react with other molecules, which leads to a reduction in the enrichment factor. To suppress this effect, we plan to use oxygen gas in forthcoming studies as a radical scavenger [47,48]. In this scheme, oxygen gas would be mixed in with $[^{11}C]CH_3I$ vapor. In addition, in the gas phase, the excitation energy of the Rydberg state is pressure-broadened by molecular collisions, which also decreases the enrichment factor. Furthermore, experiments with additional nitrogen gas are planned because we expected additional nitrogen gas to suppress the pressure-broadening effect [49]. In short, we have to optimize the gas pressure and the ratio of additional gas components. A full discussion of the suppression effects will be part of a future presentation—the next step at this point is to study the dissociation of condensed CH_3I vapor in an optical cell.

Concerning the measurement of the cross section again, the disadvantages of our present method are the possible contribution of the velocity distribution of the target molecule and the sensitivity of the method to the alignment of the pump and probe laser beams. However, the apparatus required for the proposed method is simple and the accuracy obtained is sufficient to estimate the enrichment factor. Moreover, the proposed method is also valid for nonfluorescent molecular species other than methyl iodide, provided that the molecule dissociates faster than the excitation rate and that its fragments cannot be ionized by the probe pulse. By monitoring the spatial distributions of pump and probe beams to ensure proper alignment and optimizing the conditions that determine the thermal velocity contribution of the target molecules, we should be able to increase the current accuracy of the proposed method to estimate two-photon-excitation cross sections.

6. Conclusion

Our pump–probe MPI experiment demonstrated that the two-photon-excitation cross section of the R 6*s* 3;0–0 of CH_3I contributed to increase to the specific activity (SA). The enrichment factor could be achieved by a factor of 1700 with laser separation via the hot band transition (R 6*s* $3;3_1^0$) using the presently available high-performance laser system. However, effects of collision and/or fragment reactions caused by the dissociation of the molecule in the gas phase can be factors that limit its performance. Therefore, further study is required in PET radiosynthesis environment.

Acknowledgments

We are indebted to Iwao Kanno of the National Institute of Radiological Sciences (NIRS), Japan, for his encouragement. Also, we would like to thank Jeff Kershaw of the NIRS for his comments concerning our manuscript. We would like to thank Enago (www.enago.jp) for the English language review. This study was partially supported by a consignment expense for Molecular Imaging Program on "Research Base for PET Diagnosis" from the Ministry of Education, Culture, Sports, Science and Technology (MEXT), Japan.

Appendix A. Rate equation

To consider the kinetics of a multiphoton process (via excitation) of a molecule, the rate equations of the process [17,50,51] are used. The rate equations for the (2 + 1) REMPI process are

$$\frac{dX}{dt} = \sigma_{ex}^{(2)} I^2 (A - X), \tag{A.1}$$

$$\frac{dA}{dt} = \sigma_{ex}^{(2)} I^2 (X - A) - \left\{ \frac{1}{T} + \left(\sigma_i^{(ex)} I \right) \right\} A, \tag{A.2}$$

$$\frac{dC}{dt} = \sigma_i^{(ex)} I A, \tag{A.3}$$

where X, A and C are the populations of the ground state, excited state and ionization continuum, respectively; $\sigma_i^{(ex)}$ is the ionization cross section for the transition to the excited state; and T is the excited state lifetime (dissociation). For the study reported herein, the peak photon density (I) was 3.45×10^{27} ($cm^{-2}\ s^{-1}$) and the lifetime of the excited state (6*s* Rydberg [3]) is considered to be 10^{-13}–10^{-12} s [52]. The two-photon cross sections of the excitation ($\sigma_{ex}^{(2)}$) and subsequent ionization are assumed to be 10^{-49}–10^{-48} (cm^4 s) and 10^{-19}–10^{-18} (cm^2), respectively, which we obtained by employing typical values for REMPI dynamics [53]. The parameters calculated from these inputs satisfy the condition $\sigma_{ex}^{(2)} I^2 << \sigma_i^{(ex)} I << 1/T$. In the case, the rate equations are resolved approximately as follows:

$$X(\Delta t) = \mathrm{X}(0) - \sigma_{ex}^{(2)} I^2 \Delta t. \tag{A.4}$$

We see that the dissociation rate $[-\Delta X/\Delta t]$ of the molecule corresponds to the excitation rate ($\sigma_{ex}^{(2)} I^2$). Moreover, under these conditions, the population of the ionization continuum is approximated as follows:

$$C(\Delta t) = \sigma_{ex}^{(2)} \sigma_i^{(ex)} I^3 T \Delta t. \tag{A.5}$$

Therefore, the ion yield (Q) per pulse from the reaction volume (V) of the number density (ρ) is given by

$$Q = V \rho \sigma_{ex}^{(2)} \sigma_i^{(ex)} I^3 T \Delta t. \tag{A.6}$$

For simplicity, this derivation has been based on a laser beam with a rectangular spatial distribution.

Appendix B. Spatial Gaussian model

We presume that the dilute target gas with number density (ρ) is irradiated by a focused laser pulse. The number Q of ions or excited molecules produced by the nth-order multiphoton process is calculated [54] from the peak photon density I, the effective reaction volume $V^{(n)}$, and the effective pulse duration $\tau^{(n)}$:

$$Q = \rho \sigma^{(n)} I^n V^{(n)} \tau^{(n)}. \tag{B.1}$$

Here we follow Gandhi and Bernstein [54] to introduce our approach. The effective reaction volume is described by

$$V^{(n)} = \int P_s^n(r,z) \mathrm{d}V = \int_{-\infty}^{\infty} \int_0^{\infty} P_s^n(r,z) 2\pi r \, dr \, dz, \tag{B.2}$$

where P_s is the spatial distribution function, z is the beam direction, and r is the radial distance from the beam axis. We assume that the transverse laser-intensity distribution is Gaussian. The spatial distribution function can be written as [55,56]

$$P_s(r,z) = \frac{1}{1+(az)^2} \cdot \exp\left(-\frac{r^2}{w^2\left[1+(az)^2\right]}\right), a = \frac{\lambda}{2\pi w^2}, \quad \text{(B.3)}$$

where w is the beam waist-radius, λ is the laser wavelength.

In the present study, the integral z range in Eq. (B.2) should be limited to within the diameter (L_z = 14.5 mm) of the open area of the MCP ion detector. In this range, we can assume that the Gaussian radius ($1/e$) corresponds to the beam waist radius w created by a 300-mm focal length lens and is approximately constant at the z-position within the sample cell. Therefore, Eq. (B.2) can be rewritten as

$$V^{(n)} = L_z \int_0^\infty P_s^n(r,0) 2\pi r\, dr. \quad \text{(B.4)}$$

For simplification, we define

$$P(r/w) = \exp\left[-\left(\frac{r}{w}\right)^2\right], \quad \text{(B.5)}$$

which we use to rewrite Eq. (B.4) as

$$V^{(n)} = L_z \int_0^\infty P^n\left(\frac{r}{w}\right) 2\pi r\, dr \quad \text{(B.6)}$$

Therefore, Eq. (B.1) takes the form

$$Q = \rho\sigma^{(n)} I^n \int P^n\left(\frac{r}{w}\right) 2\pi r\, dr\; L_z \tau^{(n)}. \quad \text{(B.7)}$$

Under these conditions, the effective reaction volume and the effective reaction area A_n introduced by Gandhi and Bernstein [54] as

$$\int P_s^n(r,z) dV = V_n = A_n L_n \quad \text{(B.8)}$$

become real. The dependence of the reaction volume on photon multiplicity is given as

$$V_n = \frac{V}{n}, \left(\text{or } A_n = \frac{S}{n}\right), \quad \text{(B.9)}$$

where S is the cross-sectional area of the laser beam at the beam waist:

$$S = \pi w^2. \quad \text{(B.10)}$$

Appendix C. Temporal Gaussian model

We also assume a Gaussian temporal distribution for the laser pulse. Therefore, referring to the literature [57], the effective pulse duration from Appendix B is related to the FWHM of the Gaussian pulse by

$$\tau^{(n)} = \frac{\Delta t}{\sqrt{n}} \quad \text{(C.1)}$$

References

[1] G.B. Saha, Basics of PET Imaging, Springer, New York, 2004. p. 106.
[2] P.H. Elsinga, Methods 27 (2002) 208–217.
[3] M. Allard, E. Fouquet, D. James, M. Szlosek-Pinaud, Curr. Med. Chem. 15 (2008) 235–277.
[4] C. Crouzel, B. Langstrom, V.W. Pike, H.H. Coenen, Appl. Radiat. Isotopes 38 (1987) 601–603.
[5] V. Gomez-Vallejo, J. Flop, Appl. Radiat. Isotopes 67 (2009) 111–114.
[6] M.-R. Zhang, K. Suzuki, Appl. Radiat. Isotopes 62 (2005) 447–450.
[7] R. Iwata, T. Ido, A. Ujiie, T. Takahashi, K. Ishiwata, K. Hatano, M. Sugahara, Appl. Radiat. Isotopes 39 (1988) 1–7.
[8] J. Yui, A. Hatori, K. Kawamura, K. Yanamoto, T. Yamasaki, M. Ogawa, Y. Yoshida, K. Kumata, M. Fujinaga, N. Nengaki, T. Fukumura, K. Suzuki, M.-R. Zhang, NeuroImage 54 (2011) 123–130.
[9] J. Noguchi, M.-R. Zhang, K. Yanamoto, R. Nakao, K. Suzuki, Nucl. Med. Biol. 35 (2008) 19–27.
[10] J. Noguchi, K. Suzuki, Nucl. Med. Biol. 30 (2003) 335–343.
[11] V.S. Letokhov, Ann. Rev. Phys. Chem. 28 (1977) 133–159.
[12] V.S. Letokhov, Nature 277 (1979) 605–610.
[13] D.H. Parker, R. Pandolfi, P.R. Stannard, M.A. El-Sayed, Chem. Phys. 45 (1980) 27–37.
[14] A. Wakai, K. Tsuchida, T. Fukumura, K. Suzuki, Chem. Phys. Lett. 516 (2011) 23–28.
[15] S. Felps, P. Hochmann, P. Brint, S.P. McGlynn, J. Mol. Spectrosc. 59 (1976) 355–379.
[16] W.S. Felps, J.D. Scott, S.P. McGlynn, J. Chem. Phys. 104 (1996) 419–429.
[17] P.M. Johnson, C.E. Otis, Ann. Rev. Phys. Chem. 32 (1981) 139–157.
[18] M. Sheik-Bahae, A.A. Said, T. Wei, D.J. Hagan, E.W. Van Stryland, IEEE J. Quantum Electron. 26 (1990) 760–769.
[19] C. Wang, L. Liu, W. Ma, Z. Zhou, G. Wang, Z. Xu, Optik 116 (2005) 75–79.
[20] C. Xu, W.W. Webb, J. Opt. Am. B 13 (1996) 481–491.
[21] M.V. Ashikhmin, Yu.E. Belyaev, A.V. Dem'yanenko, E.A. Ryabov, V.S. Letokhov, Chem. Phys. Lett. 227 (1994) 343–348.
[22] J.L. Knee, L.R. Khundkar, A.H. Zewail, J. Chem. Phys. 83 (1985) 1996–1998.
[23] L.R. Khundkar, A.H. Zewail, Annu. Rev. Phys. Chem. 41 (1990) 15–60.
[24] Y. Wang, H. Shen, L. Hua, C. Hu, B. Zhang, Opt. Express 17 (2009) 10506–10513.
[25] D.H. Parker, M.A. El-Sayed, Chem. Phys. 42 (1979) 379–387.
[26] L. Poth, Q. Zhong, J.V. Ford, A.W. Castleman Jr., J. Chem. Phys. 109 (1998) 4791–4797.
[27] A.P. Baranavski, J.C. Owrutsky, J. Chem. Phys. 108 (1998) 3445–3452.
[28] D. Zhong, A.H. Zewail, J. Phys. Chem. A 102 (1998) 4031–4058.
[29] G. Gizinger, M.E. Corrales, V. Loriot, G.A. Amaral, R. de Nalda, L. Bañares, J. Chem. Phys. 132 (2010) 234313.
[30] P. Brewer, P. Das, G. Ondrey, R. Bersohn, J. Chem. Phys. 79 (1983) 720–723.
[31] H. Kojima, T. Fukumi, S. Nakajima, Y. Maruyama, K. Kosaka, Chem. Phys. Lett. 95 (1983) 614–617.
[32] J.H. Clark, Y. Haas, P.L. Houston, C.B. Moore, Chem. Phys. Lett. 35 (1975) 82–85.
[33] R.V. Ambartzumian, N.P. Furzikov, Yu.A. Gorokhov, V.S. Letokhov, G.N. Makarov, A.A. Puretzky, Opt. Commun. 18 (1976) 517–521.
[34] G. Hancock, J.D. Campbell, K.H. Welge, Opt. Commun. 16 (1976) 177–181.
[35] A. Fahr, A.K. Nayak, M.J. Kurylo, Chem. Phys. 197 (1995) 195–203.
[36] J. Tellinghuisen, Adv. Chem. Phys. 60 (1985) 299–368.
[37] H. Guo, A.H. Zewail, Can. J. 72 (1994) 947.
[38] Y.-K. Choi, Y.-M. Koo, K.-W. Jung, J. Photochem. Photobiol., A 127 (1999) 1–5.
[39] Y. Jiang, M.R. Giorigi-Arnazzi, R.B. Bernstein, Chem. Phys. 106 (1986) 171–178.
[40] A.B. Alekseyev, H.-P. Lebermann, R.J. Buenker, J. Chem. Phys. 134 (2011) 044303. They did not study the 6*s* Rydberg [3] state of CH_3I. We decided to use excited iodine by analogy of R 6*s* [4] and [2] in Fig. 2 in the their report.
[41] D.W. Chandler, J.W. Thoman Jr., Chem. Phys. Lett. 156 (1989) 151–158.
[42] S. Matsuura, S. Umebayashi, C. Okuyama, K. Oba, IEEE Trans. Nucl. Sci. NS-32 (1985) 350–354.
[43] O.V. Rattigan, E.E. Shallcross, R.A. Cox, J. Chem, Soc. Faraday Trans. 93 (1997) 2839–2846.
[44] H. Guo, A.H. Zewail, Can. J. Chem. 72 (1994) 947–957.
[45] B. Urban, V.E. Bondybey, J. Chem. Phys. 116 (2002) 4938–4947.
[46] R.L. Swofford, W.M. McClain, Chem. Phys. Lett. 34 (1975) 455–460.
[47] J. Heicklen, H.S. Johnston, J. Am. Chem. Soc. 84 (1962) 4030–4039.
[48] J. Farren, J.R. Gilbert, J.W. Linnett, I.A. Read, J. Chem. Soc. Trans. Faraday 60 (1964) 740–750.
[49] U. Asaf, K. Rupnik, G. Reisfeld, S.P. McGlynn, J. Chem. Phys. 99 (1993) 2560–2566.
[50] D.S. Zakheim, P.H. Johnson, Chem. Phys. 46 (1980) 263–272.
[51] B. Zheng, M. Lin, B. Zhang, W. Chen, Opt. Commun. 73 (1989) 208–212.
[52] D.J. Campbell, L.D. Ziegler, Chem. Phys. Lett. 201 (1993) 159–165.
[53] D.H. Parker, J.O. Berg, M.A. El-Sayed, in: A.H. Zewail (Ed.), Advances in Laser Chemistry (Springer series in Chemical Physics 3), Springer, Berlin, Heidelberg, New York, 1978, pp. 320–335.
[54] S.R. Gandhi, R.B. Bernstein, Chem. Phys. 105 (1986) 423–434.
[55] M.V. Ammosov, N.B. Delone, M.Yu. Ivanov, Adv. Atom., Mol., Opt. Phys. 29 (1992) 33–110.
[56] A. L'Huillier, L.A. Lompre, G. Mainfray, C. Manus, J. Phys. B: Atom. Mol. Opt. Phys. 16 (1983) 1363–1381.
[57] D. Normand, J. Morellec, J. Phys. B: Atom. Mol. Phys. 13 (1980) 1551–1561.

Original Paper

Cerebrovascular Diseases

Cerebrovasc Dis
DOI: 10.1159/000332034

Received: February 24, 2011
Accepted: August 15, 2011
Published online: ■■■

Safety of Low-Frequency Transcranial Ultrasound in Permanent Middle Cerebral Artery Occlusion in Spontaneously Hypertensive Rats

Zuojun Wang[a, d] Takahiro Fukuda[b] Takashi Azuma[c] Hiroshi Furuhata[a]

[a]Medical Engineering Laboratory, [b]Division of Neuropathology, Research Center for Medical Sciences, Jikei University School of Medicine, and [c]Department of Biomedical Research, Faculty of Engineering, University of Tokyo, Tokyo, Japan; [d]Department of Ultrasonic Medicine, Tangdu Hospital, Fourth Military Medical University, Xi'an, China

Key Words

Acute stroke · Cerebral ischemia · Experimental stroke research · Intracranial hemorrhage · Hypertension · Thrombolysis · Ultrasound

Abstract

Background: Some studies suggest that low-frequency transcranial ultrasound (LFTUS) can enhance thrombolysis, but other studies suggest that it may have adverse effects on intracranial tissues. We previously reported that LFTUS with appropriate parameters was effective and safe in a normotensive rat model of thromboembolic middle cerebral artery occlusion (MCAO) stroke. The goal of this study was to test the safety of this strategy in a spontaneously hypertensive rat (SHR) model of permanent MCAO. ***Methods:*** Right MCAO was achieved in male SHRs using intraluminal nylon sutures. Rats exhibiting left hemiparesis were randomly assigned to one of four different groups: (1) normal saline (NS) group (n = 8), intravenous administration of NS as placebo at 3 h after MCAO; (2) NS+LFTUS group (n = 10), NS administration with simultaneous application of LFTUS (480.4 kHz, continuous wave, at an intensity of 0.3 W/cm^2) for 1 h; (3) tissue plasminogen activator (tPA) group (n = 11), intravenous administration of alteplase (10 mg/kg body weight) over 1 h instead of NS; or (4) tPA+LFTUS group (n = 11), tPA administration and application of LFTUS. Twenty-four hours after treatment, neurological change was evaluated, and brains were removed and examined histologically. ***Results:*** There was no significant difference ($p > 0.09$) when comparing changes in neurologic status and body weight, infarct ratio, edema ratio, or hemorrhagic transformation among the four groups. ***Conclusions:*** Our findings suggest that sonothrombolytic treatment with LFTUS with appropriate parameters is safe when used for the treatment of ischemic stroke in hypertensive rats under the undesired permanent MCAO condition.

Introduction

The thrombolytic efficacy of transcranial ultrasound in the treatment of acute ischemic stroke (AIS) [1–6] has attracted a great deal of attention among stroke investigators. Indeed, low-frequency ultrasound enhances the thrombolytic effect of other modalities [7–10] and has good skull penetration [11–13]. However, the TRUMBI trial demonstrated that low-frequency transcranial ultrasound (LFTUS) is associated with a very high rate of symptomatic intracranial hemorrhages in patients with AIS [14]. Studies performed to investigate the reasons for these complications [15–18] suggest that hemorrhage

KARGER

Fax +41 61 306 12 34
E-Mail karger@karger.ch
www.karger.com

1015–9770/11/0000–0000$38.00/0

Accessible online at:
www.karger.com/ced

Zuojun Wang, MD
Medical Engineering Laboratory
Jikei University School of Medicine
3-25-8 Nishi-shinbashi, Minato-ku, Tokyo 105-8461 (Japan)
Tel. +81 3 3433 1111, ext. 2338, E-Mail wangzj@jikei.ac.jp